Citation for published version:
Chew, J 2004, 'CFD Studies of Dynamic Gauging', Chemical Engineering Science, vol. 59, no. 16, pp. 3381-3398. https://doi.org/10.1016/j.ces.2004.03.042

DOI:
10.1016/j.ces.2004.03.042

Publication date:
2004

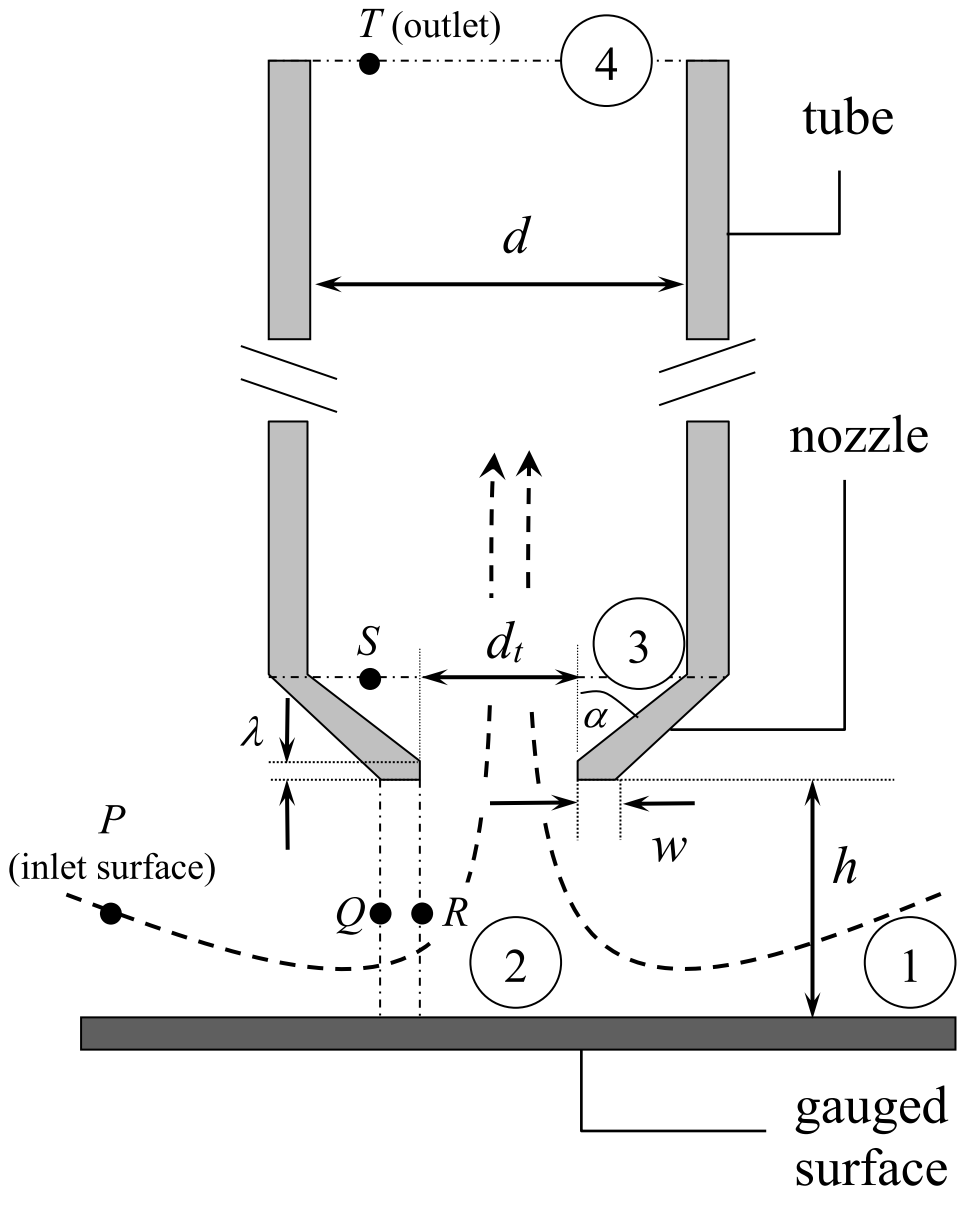

Figure 1: Schematic of a typical gauging nozzle showing dimensions.

a) **1** – **4** are flow stations.

b) *P* – *T* are points showing the different sections for pressure drop analysis (*PQ* – convergent section, *QR* – area under the rim, *RS* – divergent section, *ST* – tube section).

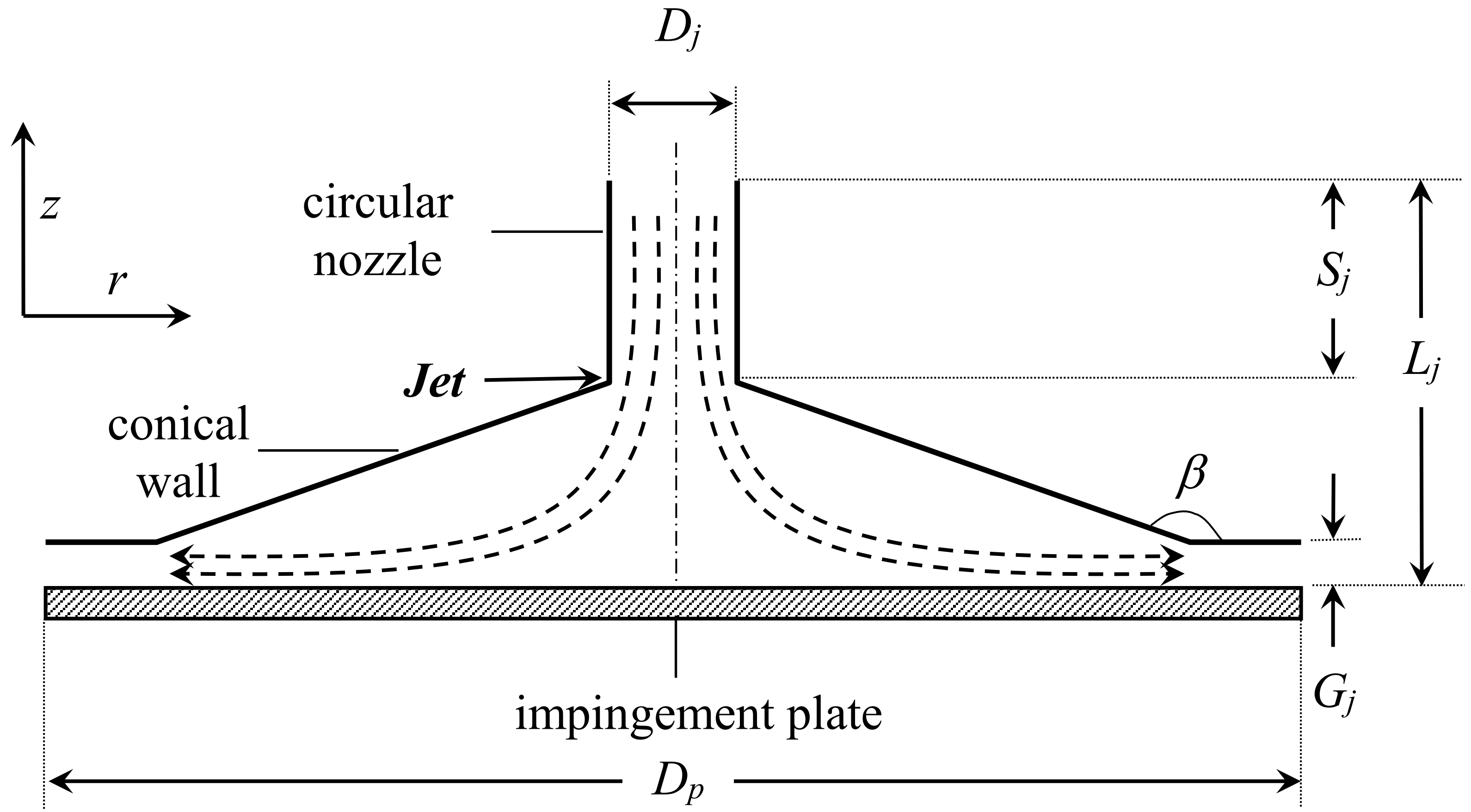

Figure 2: Schematic of a conical cell showing the ratios of dimensions.
(D_p/D_j = 8, L_j/D_j = 1, S_j/D_j = 0.35, G_j/D_j = 0.1, β = 168.9°)

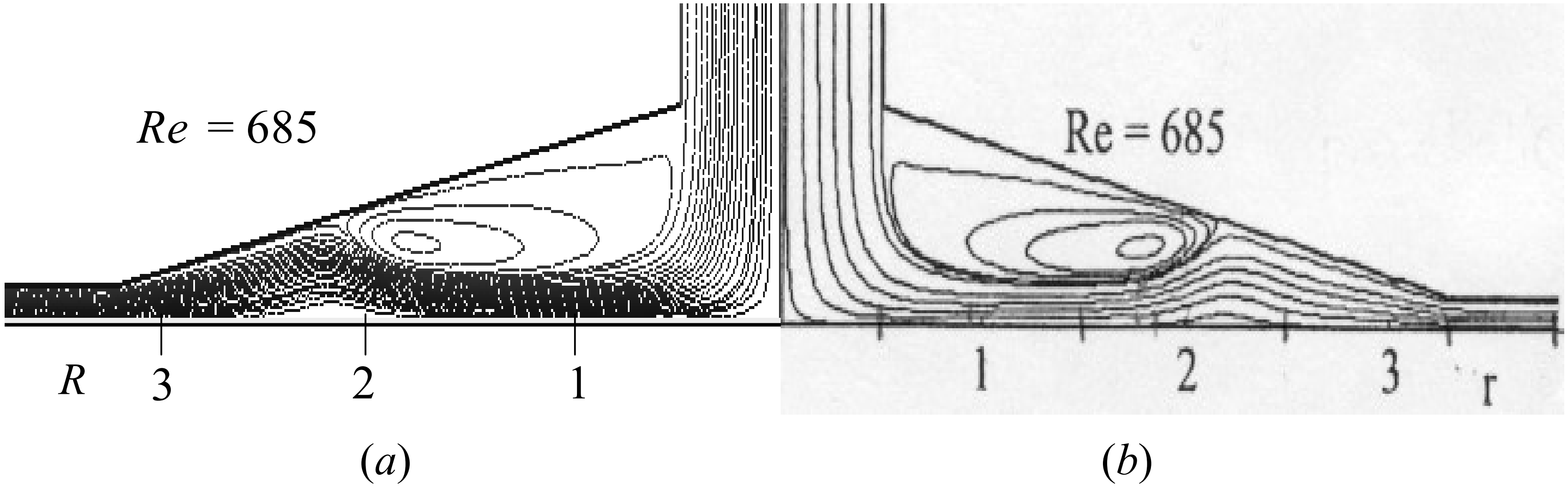

Figure 3: Comparison of predicted streamlines at $Re = 685$.
(*a*) – this work, (*b*) – Miranda & Campos (1999).

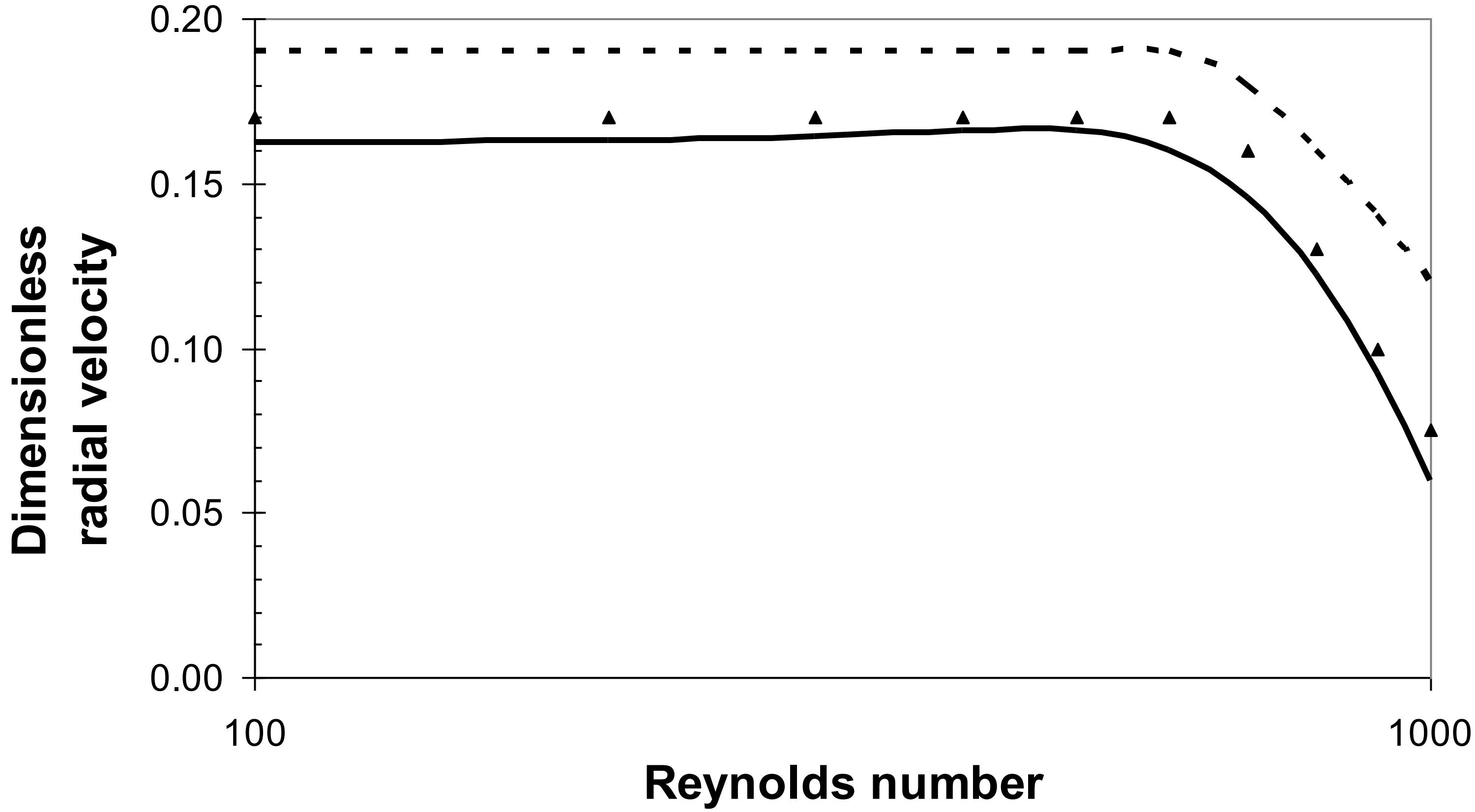

Figure 4: Comparison of radial velocities at one point within the conical cell, $R = 2.65$, $Z = 0.034$.
Solid line – this work; squares – experimental data (Miranda & Campos, 1999); dotted line – numerical predictions (finite difference, Miranda & Campos, 1999).

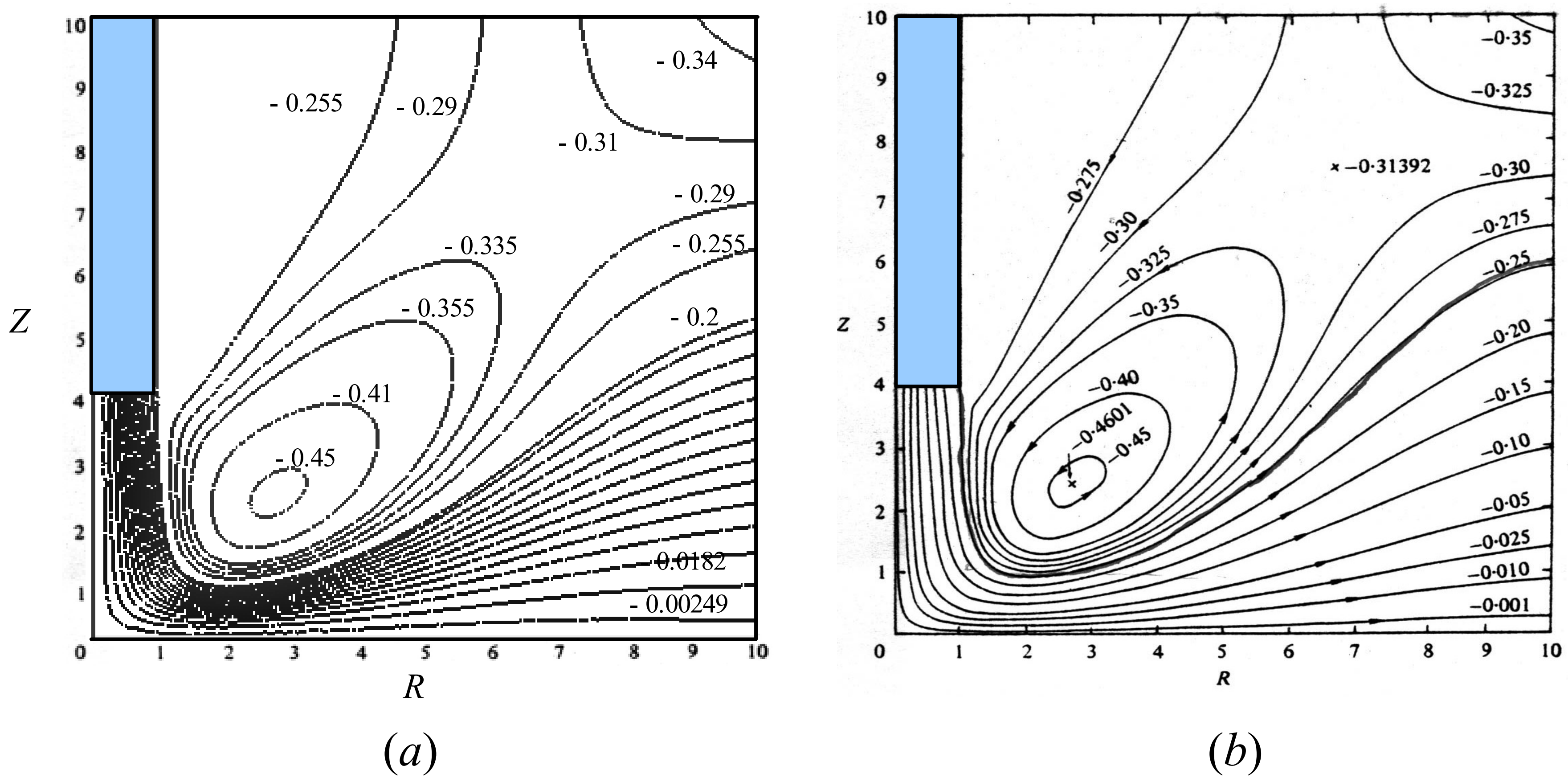

Figure 5: Comparison of streamline predictions for impinging laminar submerged jet at *Re* = 25, defined at the jet exit. (*a*) – this work, (*b*) – Deshpande & Vaishnav (1982).

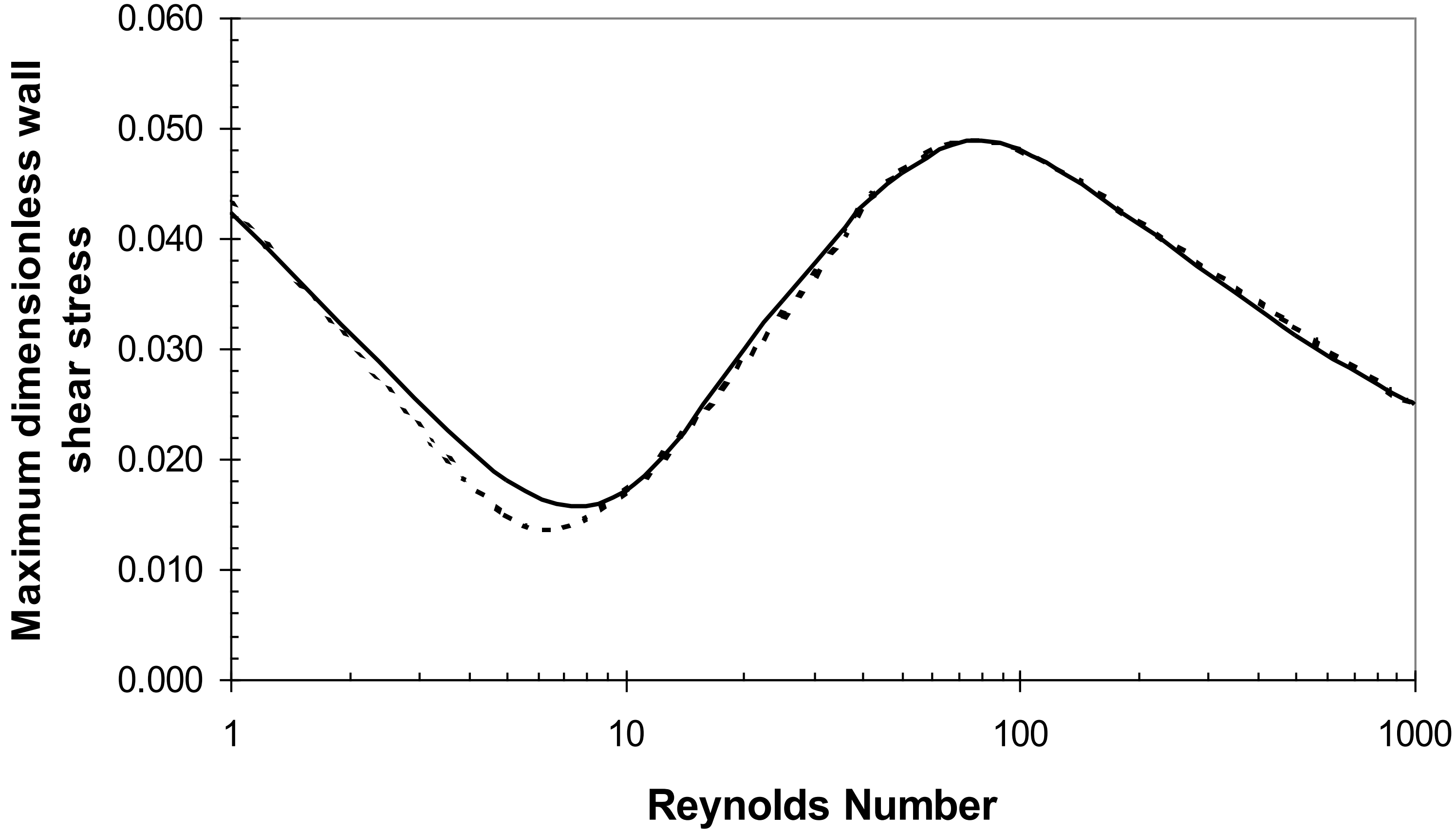

Figure 6: Comparison of predictions of the maximum dimensionless wall shear stress for an impinging laminar jet. Solid line – this work; dotted line –Deshpande & Vaishnav (1982).

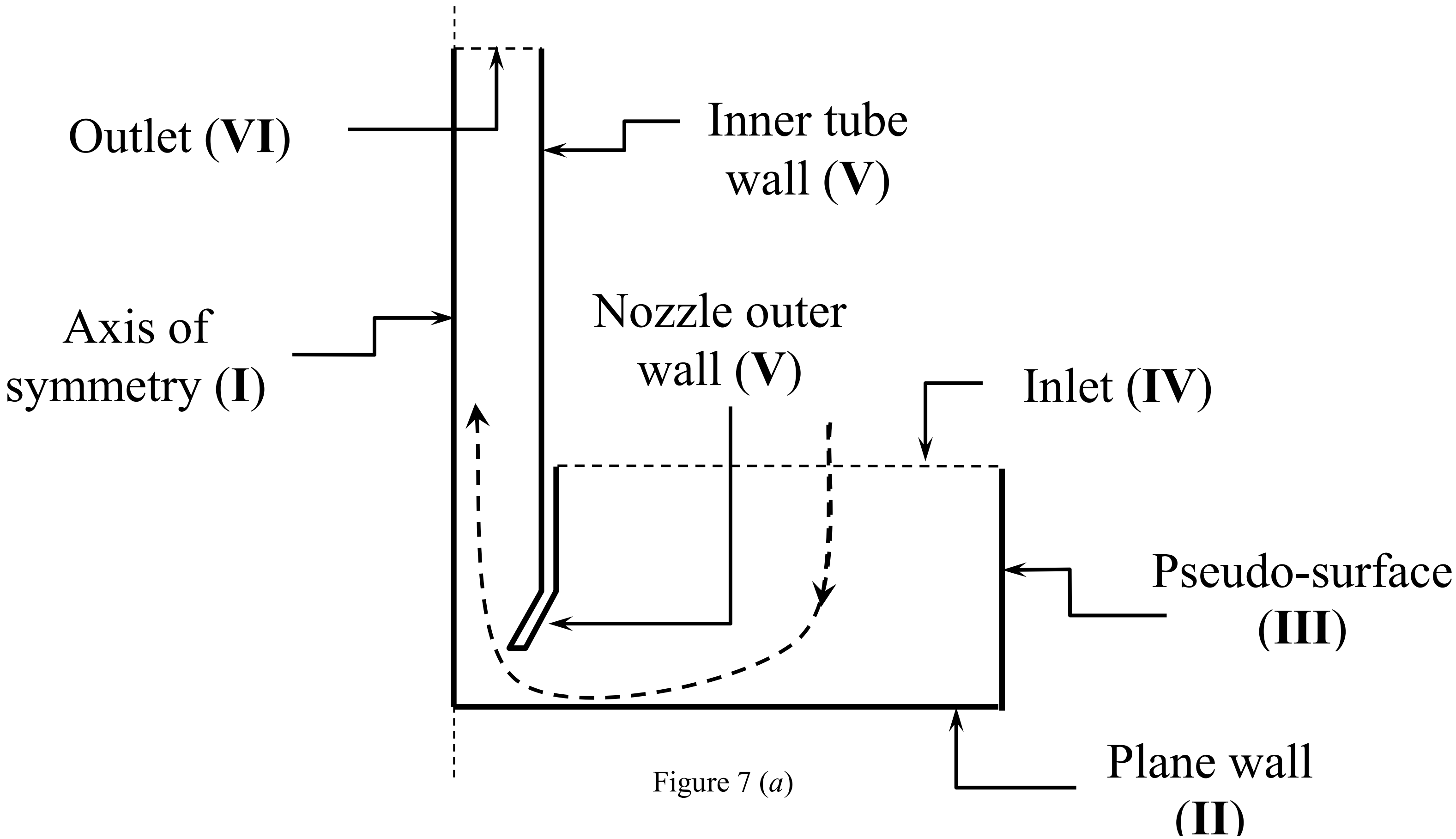

Figure 7 (*a*)

Figure 7: Computational models for different inlet boundary conditions. Boundary tags **I** to **VI** are shown in brackets. (*a*) – Model 1, (*b*) – Model 2, (*c*) – Model 3.

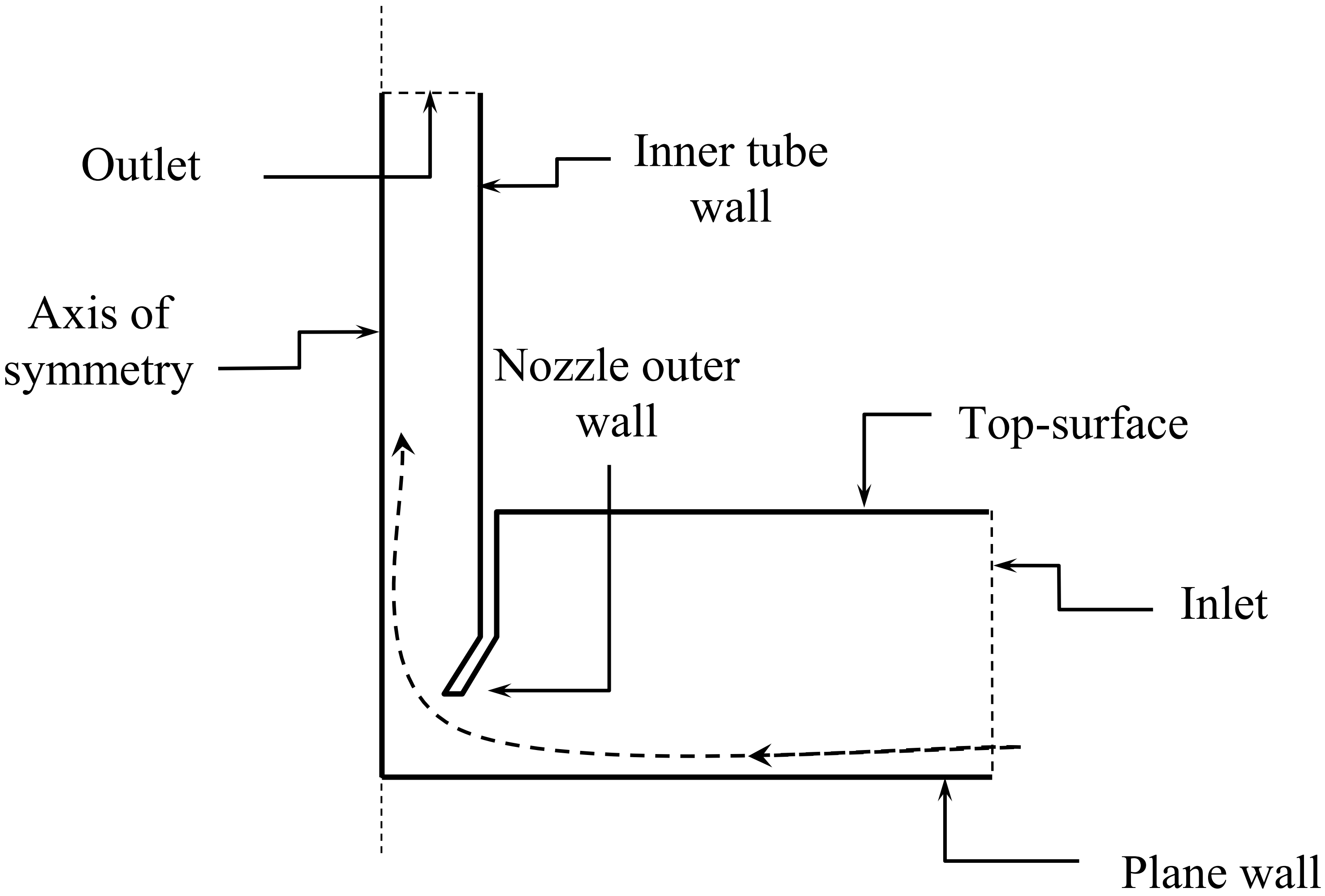
Outlet
Inner tube wall
Axis of symmetry
Nozzle outer wall
Top-surface
Inlet
Plane wall

Figure 7 (*b*)

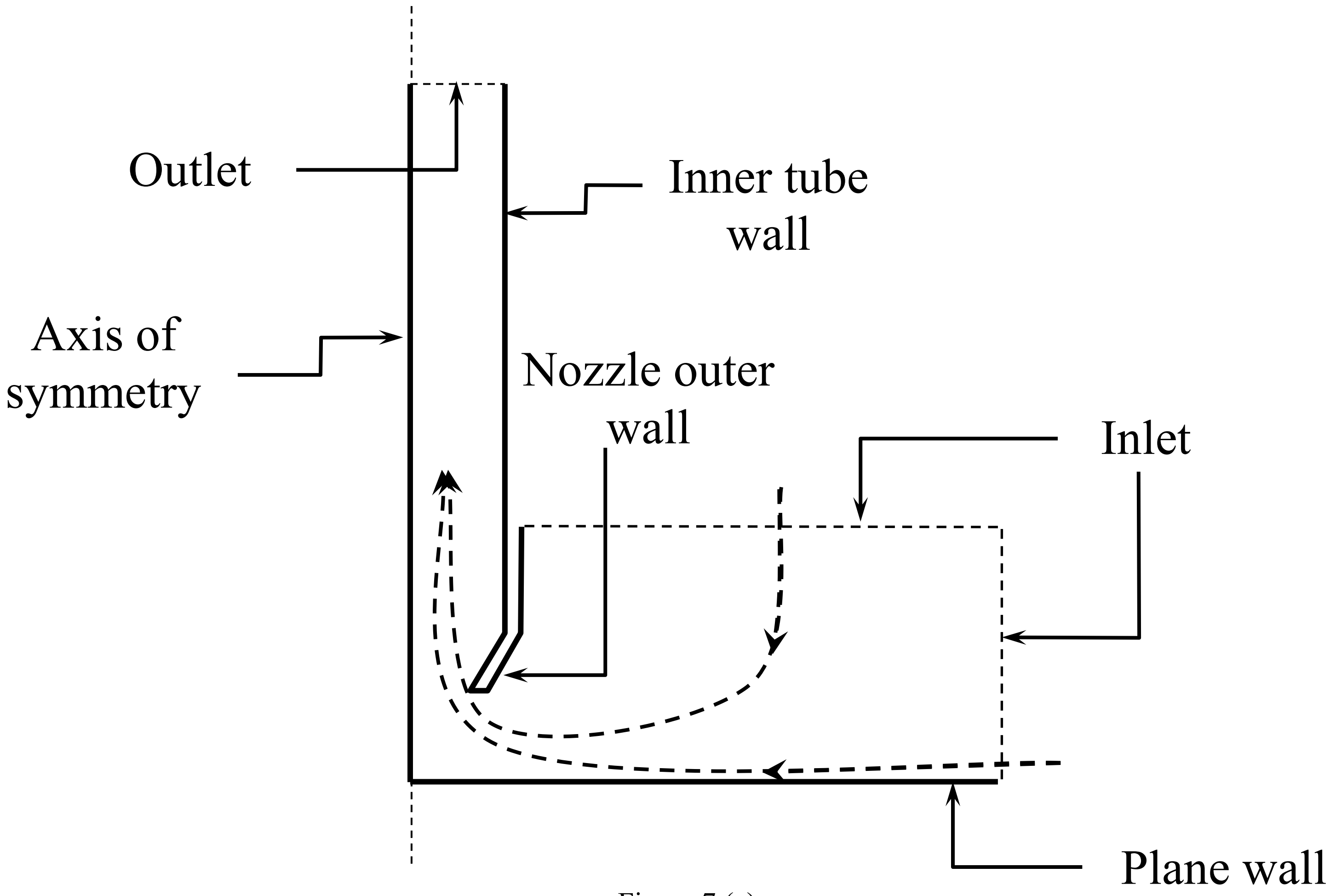
Outlet
Inner tube wall
Axis of symmetry
Nozzle outer wall
Inlet
Plane wall

Figure 7 (*c*)

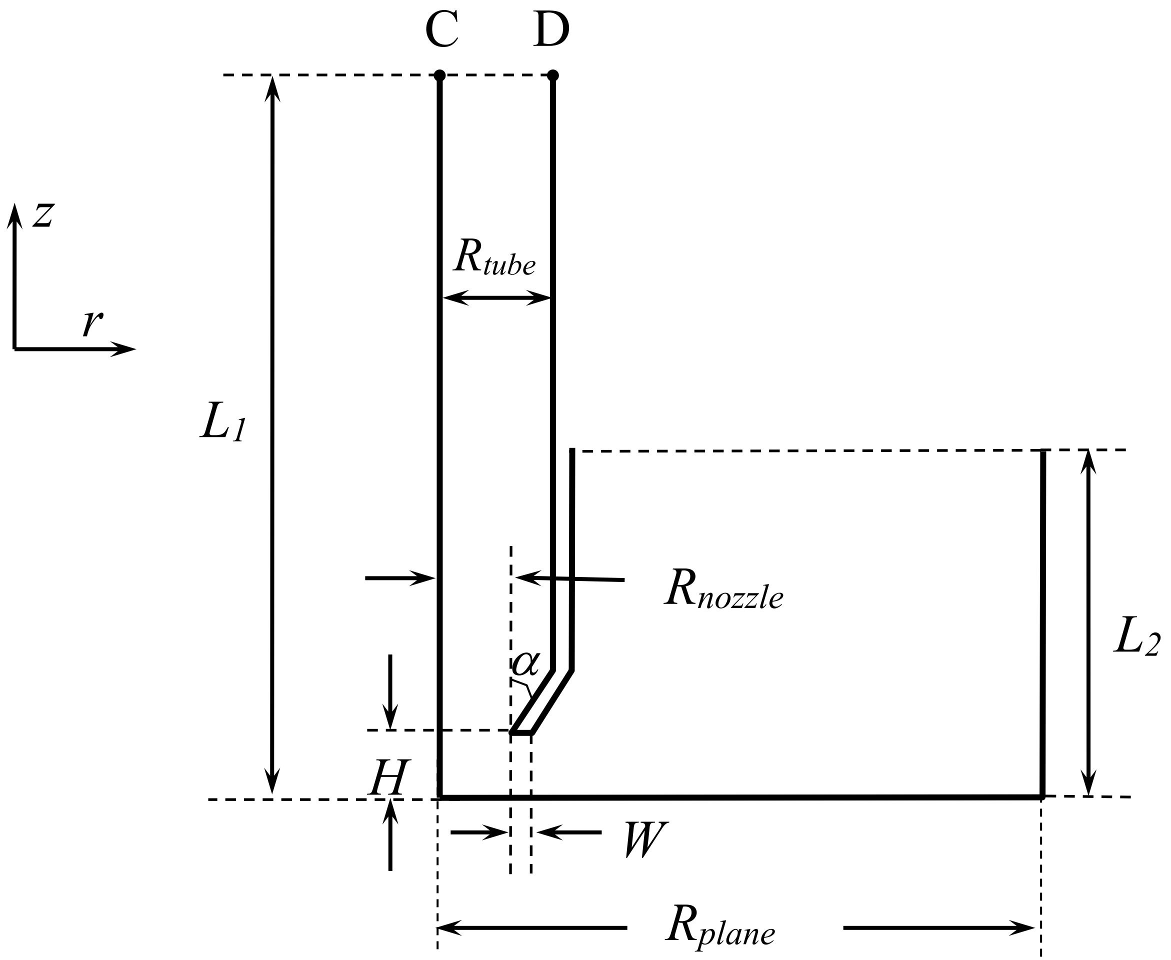

Figure 8: Dimensionless coordinates of the gauging nozzle (R_{tube} = 1).

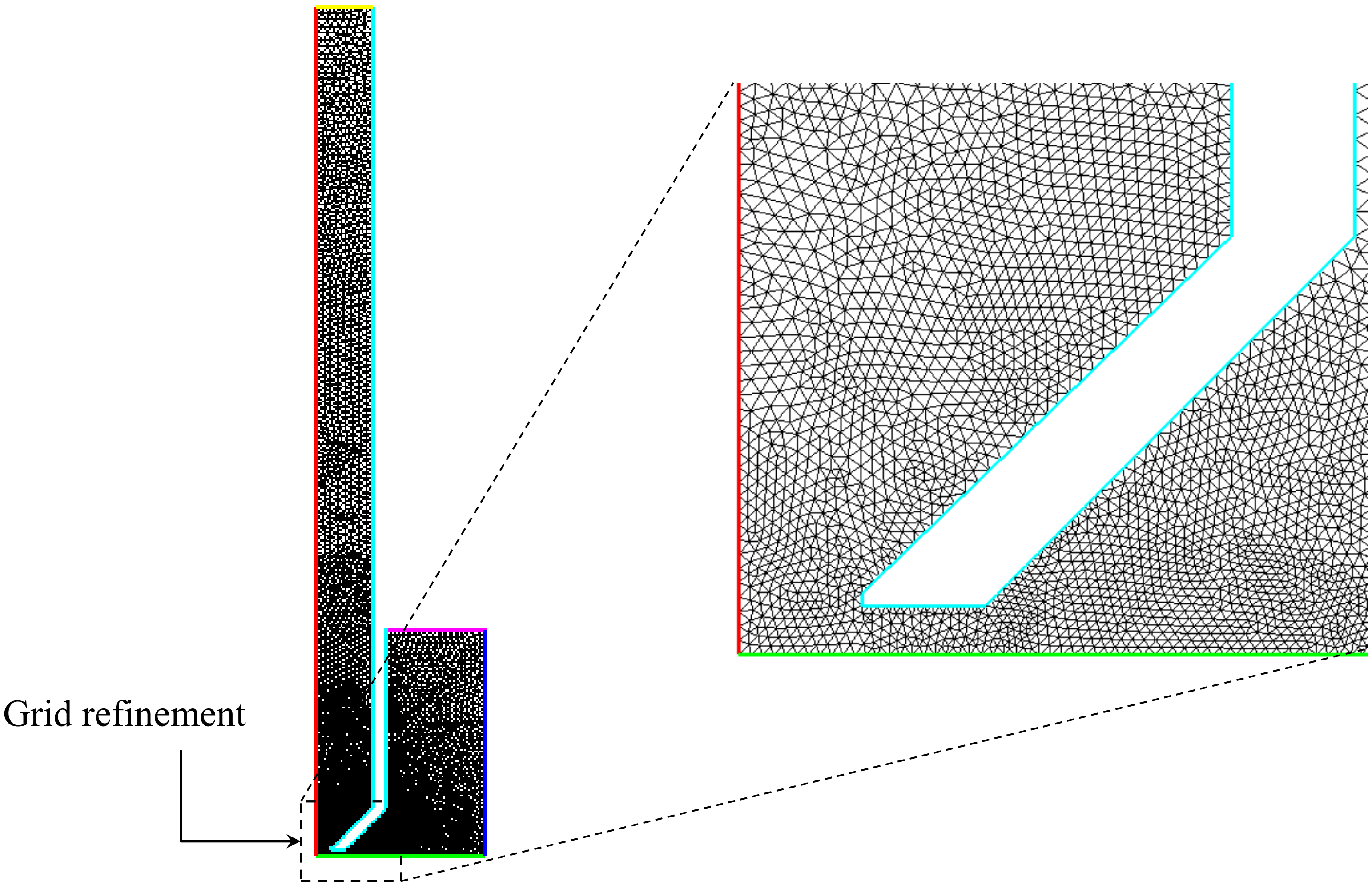

Figure 9: Grid refinement in the region near the nozzle for a typical simulation case.

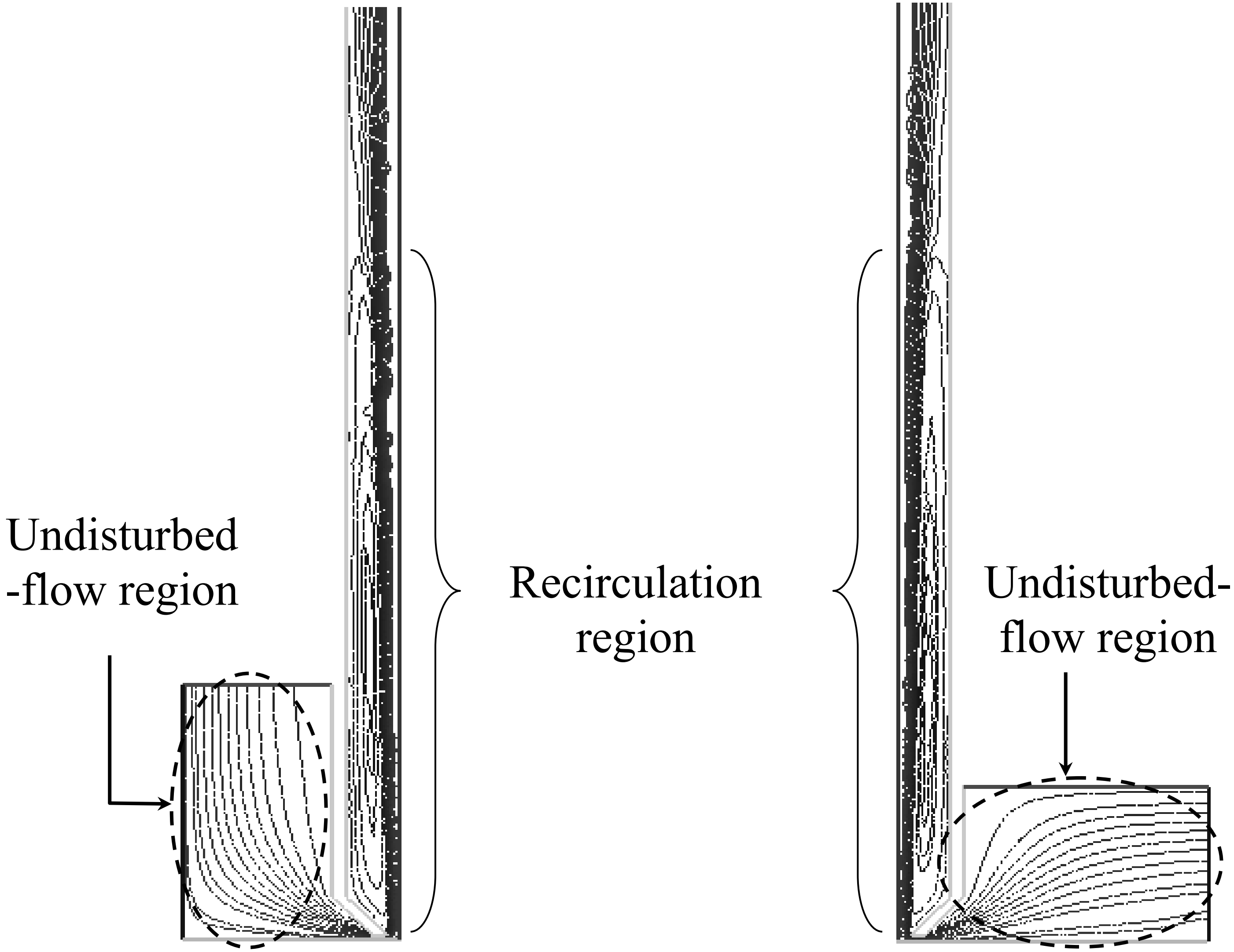

10 (*a*): Model 1

10 (*b*): Model 2

Figure 10: Streamlines at $Re_t = 260$ and $h/d_t = 0.125$ showing three distinct flow regions. (*a*) – Model 1, (*b*) – Model 2, (*c*) – Model 3, (*d*) – Suction region.

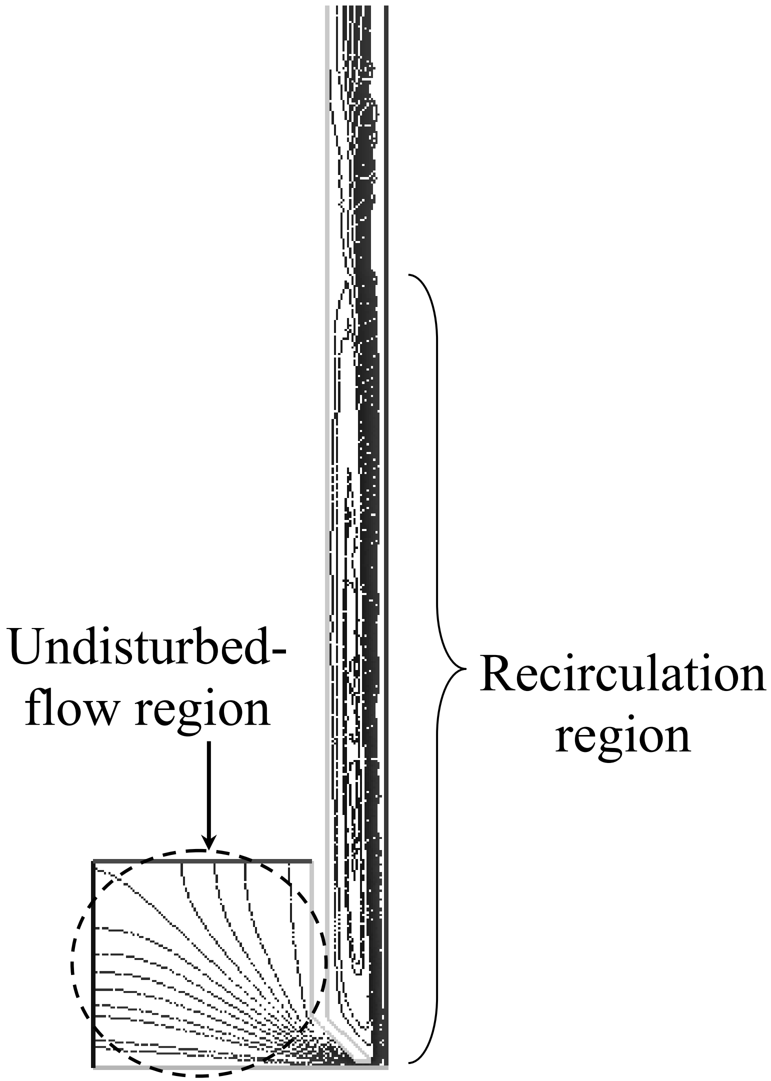

10 (*c*): Model 3

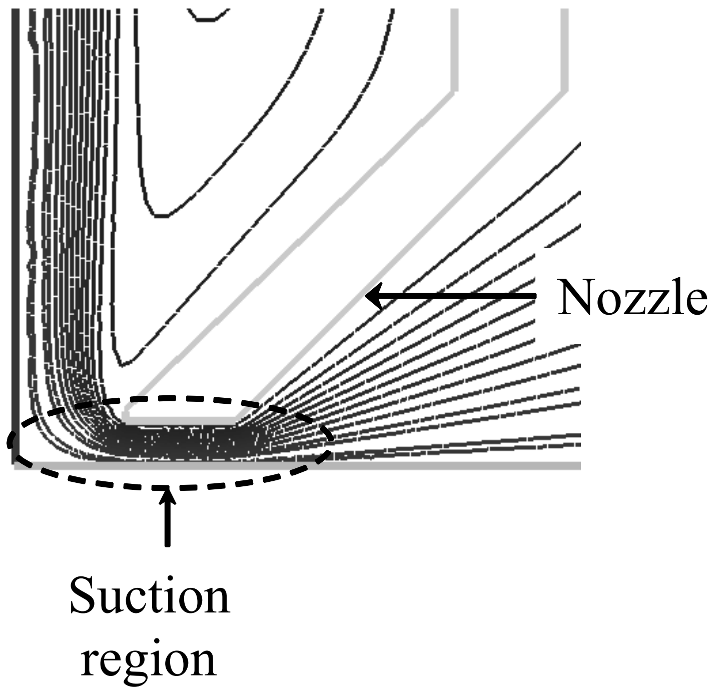

Figure 10 (*d*): Suction region

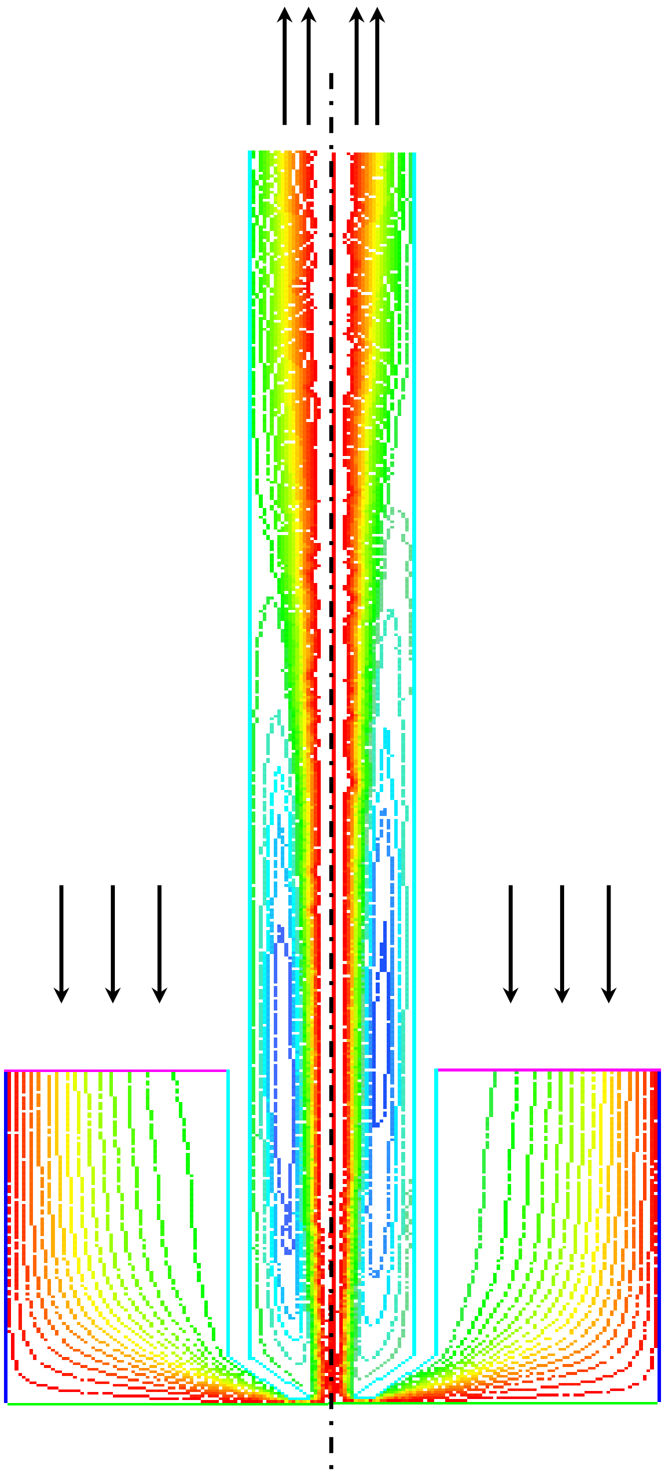

Figure 11(a): Streamlines from Model 1 at $h/d_t = 0.2$ and $Re_t = 160$ (left) and 200 (right).

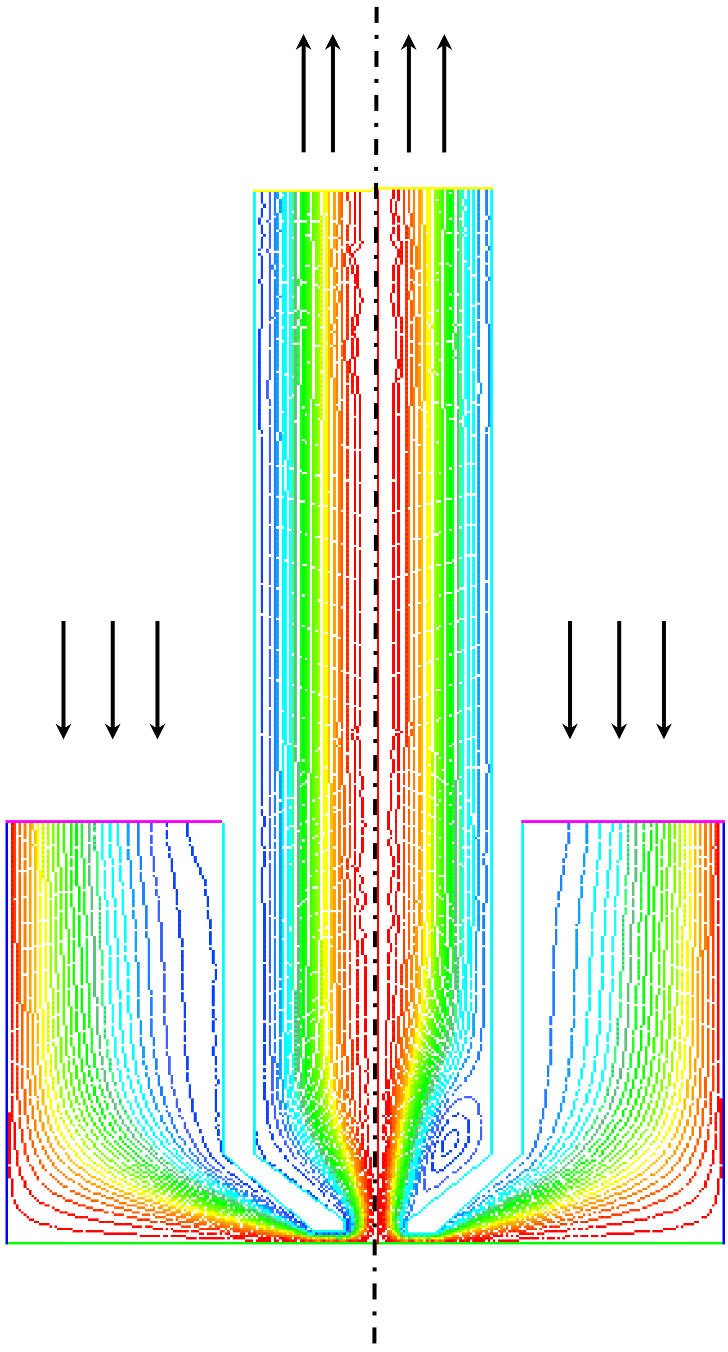

Figure 11(b): Streamlines from Model 1 at $h/d_t = 0.2$ and $Re_t = 8$ (left) and 20 (right).

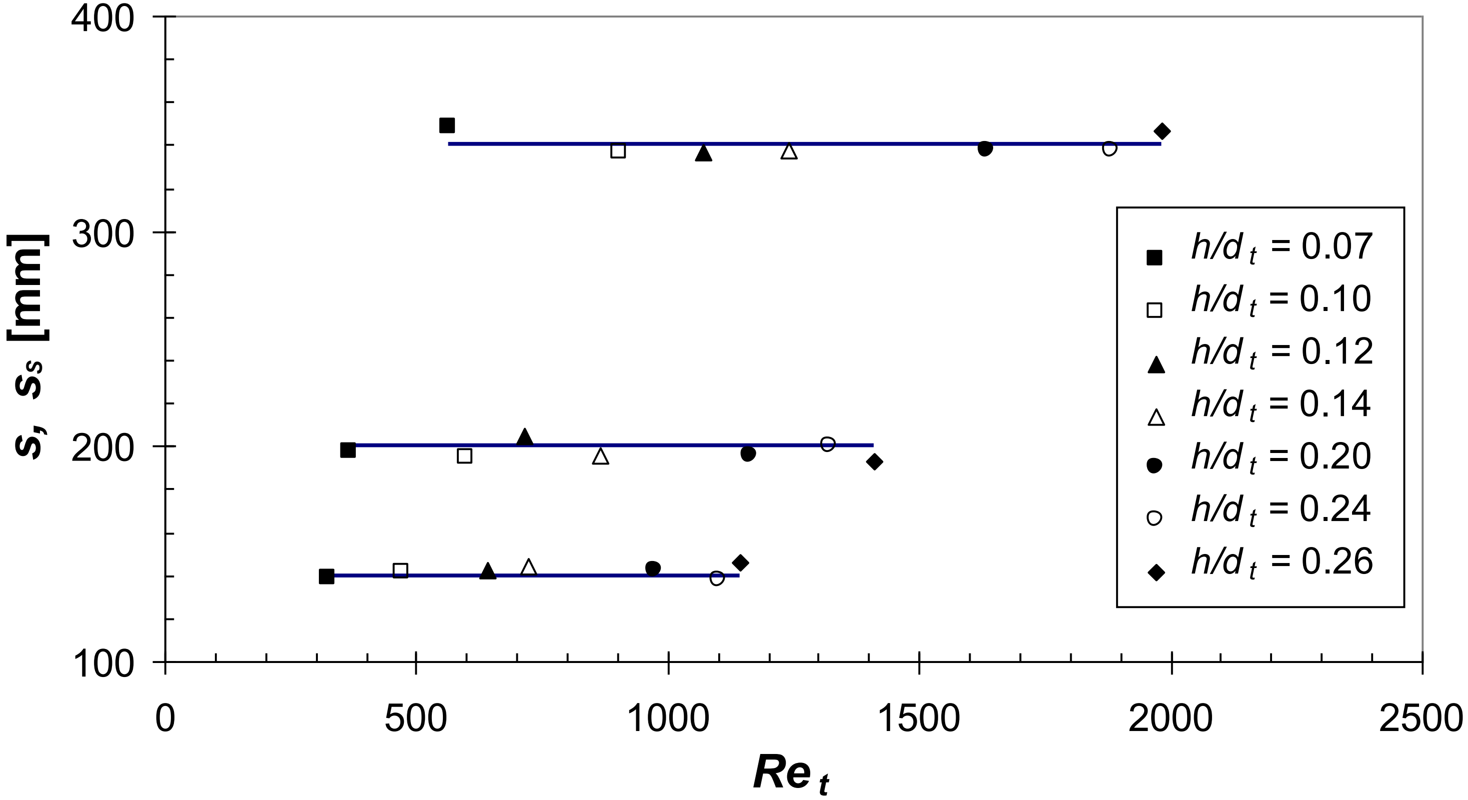

Figure 12: Comparison of hydrostatic head for gauging flows (water).
Symbols - simulation s_s; solid line - experimental s.

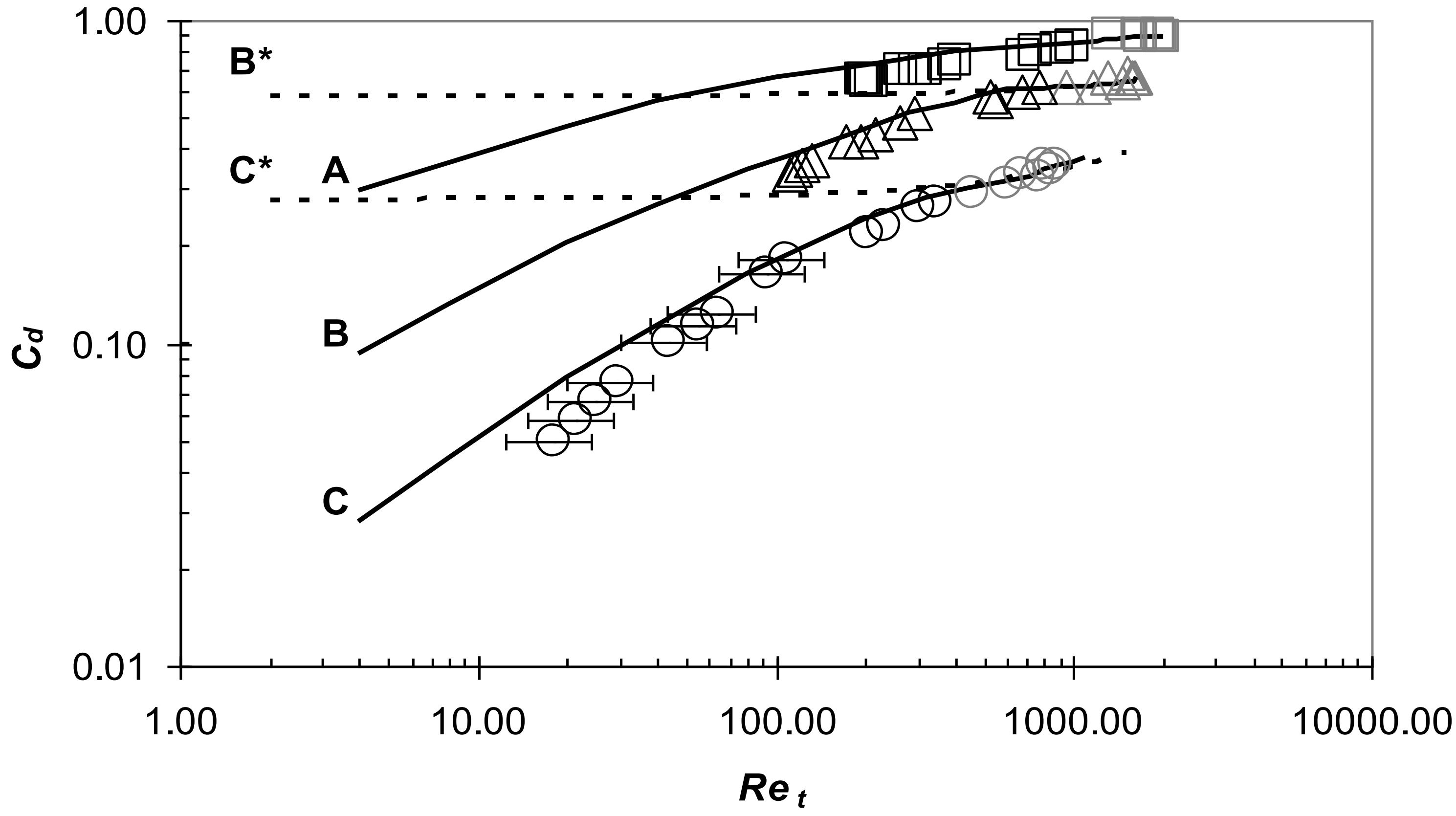

Figure 13(*a*): Discharge coefficient versus Re_t.
Solid lines – this work; **A** – $h/d_t = 0.65$, **B** – $h/d_t = 0.20$, **C** – $h/d_t = 0.10$; symbols – experimental data, black – this work, grey – (Tuladhar, 2001); squares – $h/d_t = 0.65$, triangles – $h/d_t = 0.20$, circles – $h/d_t = 0.10$; dotted lines – empirical model from Tuladhar et al. (2000) – equation (19); **B*** – $h/d_t = 0.20$, **C*** – $h/d_t = 0.10$.
Nozzle: $d_t = 1$ mm, $d = 4$ mm, $w = 0.5$ mm, $\lambda = 0.1$ mm and $\alpha = 45^o$.

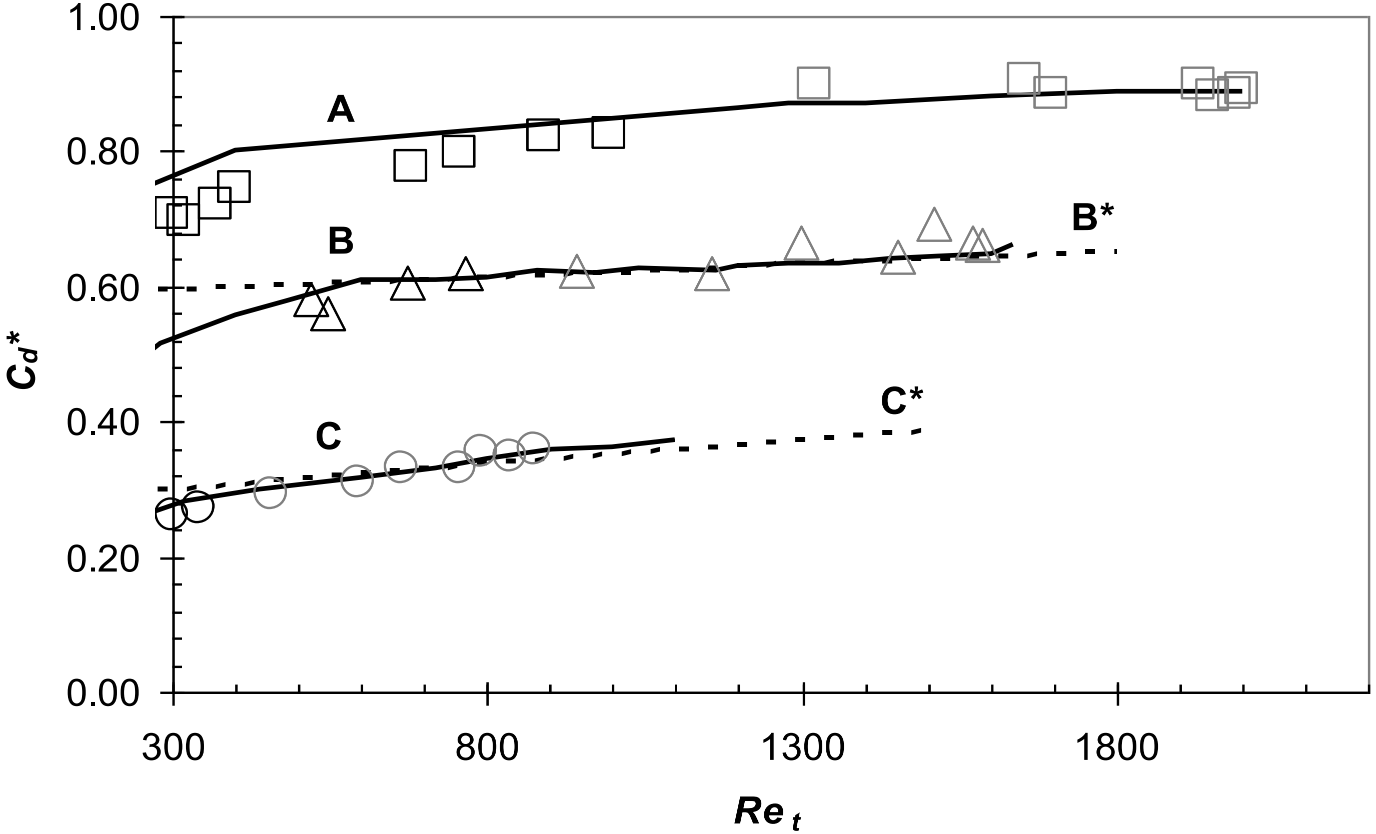

Figure 13(*b*): Asymptotic discharge coefficient versus Re_t, high Re_t range.
Solid lines – this work; **A** – $h/d_t = 0.65$, **B** – $h/d_t = 0.20$, **C** – $h/d_t = 0.10$; symbols – experimental data, black – this work, grey – (Tuladhar, 2001); squares – $h/d_t = 0.65$, triangles – $h/d_t = 0.20$, circles – $h/d_t = 0.10$; dotted lines – empirical model from Tuladhar *et al*. (2000) – equation (19); **B*** – $h/d_t = 0.20$, **C*** – $h/d_t = 0.10$.
Nozzle: $d_t = 1$ mm, $d = 4$ mm, $w = 0.5$ mm, $\lambda = 0.1$ mm and $\alpha = 45^o$.

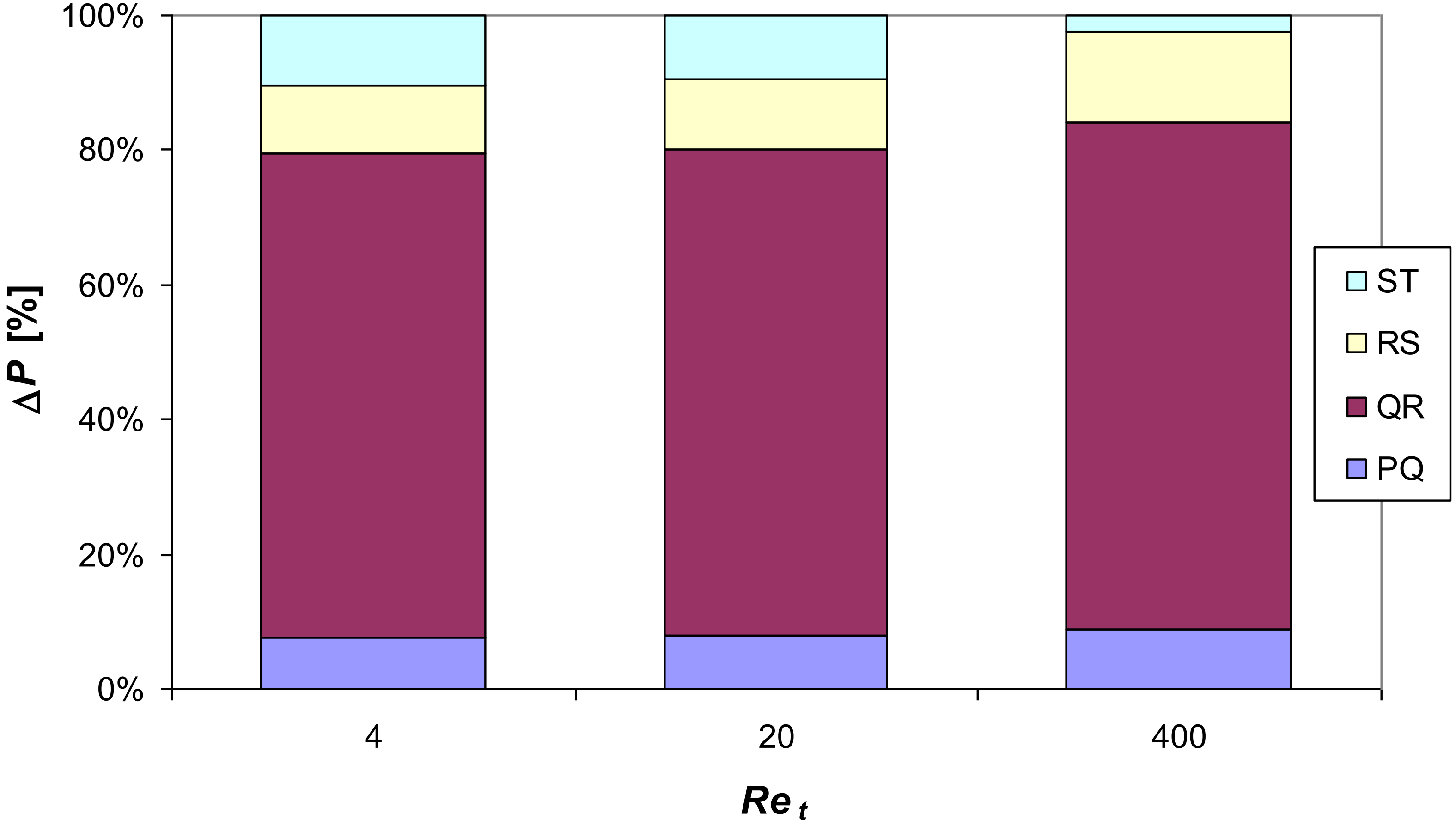

Figure 14 (*a*): Pressure drop analysis, h/d_t = 0.10.

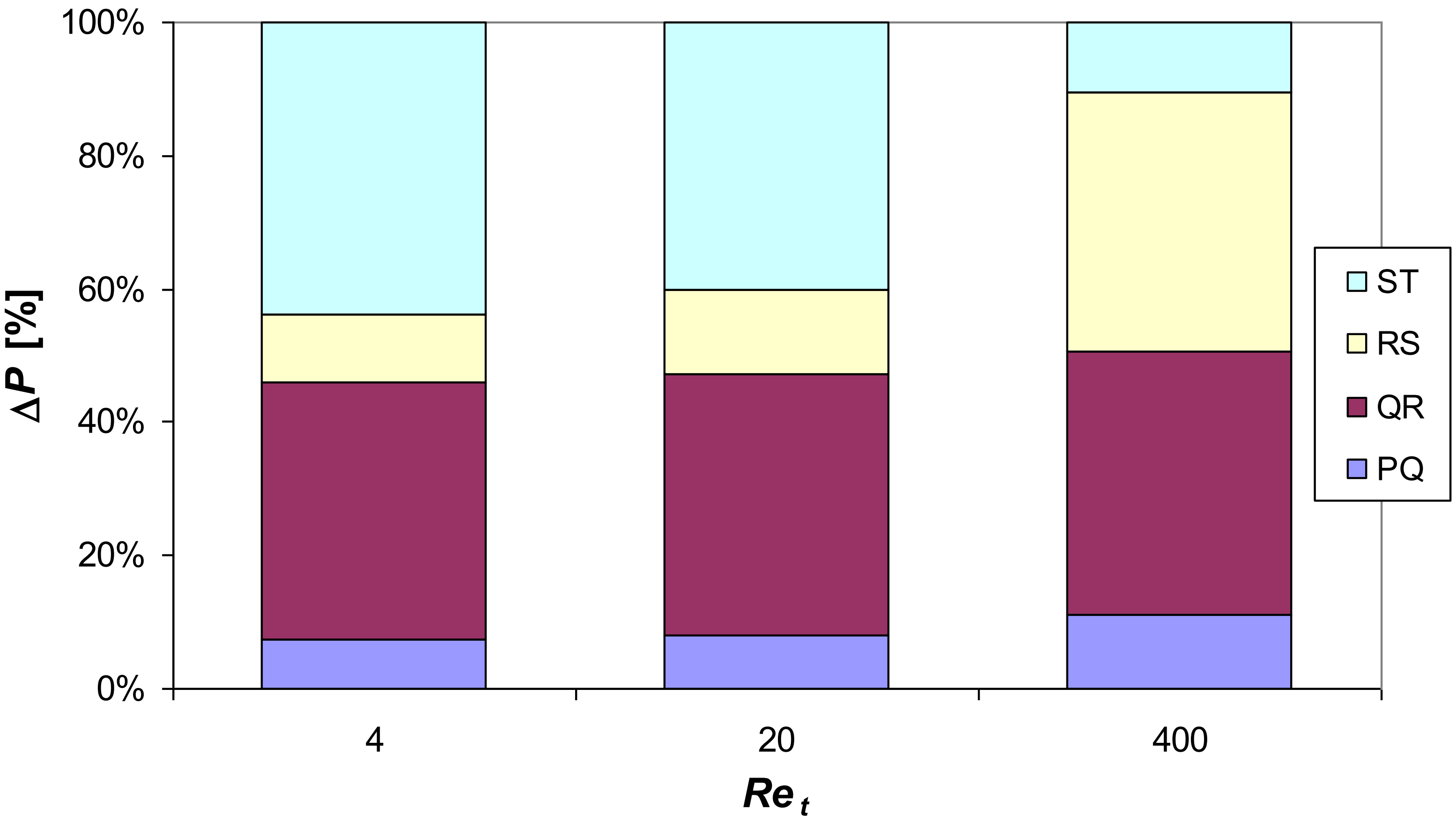

Figure 14 (*b*): Pressure drop analysis, $h/d_t = 0.20$.

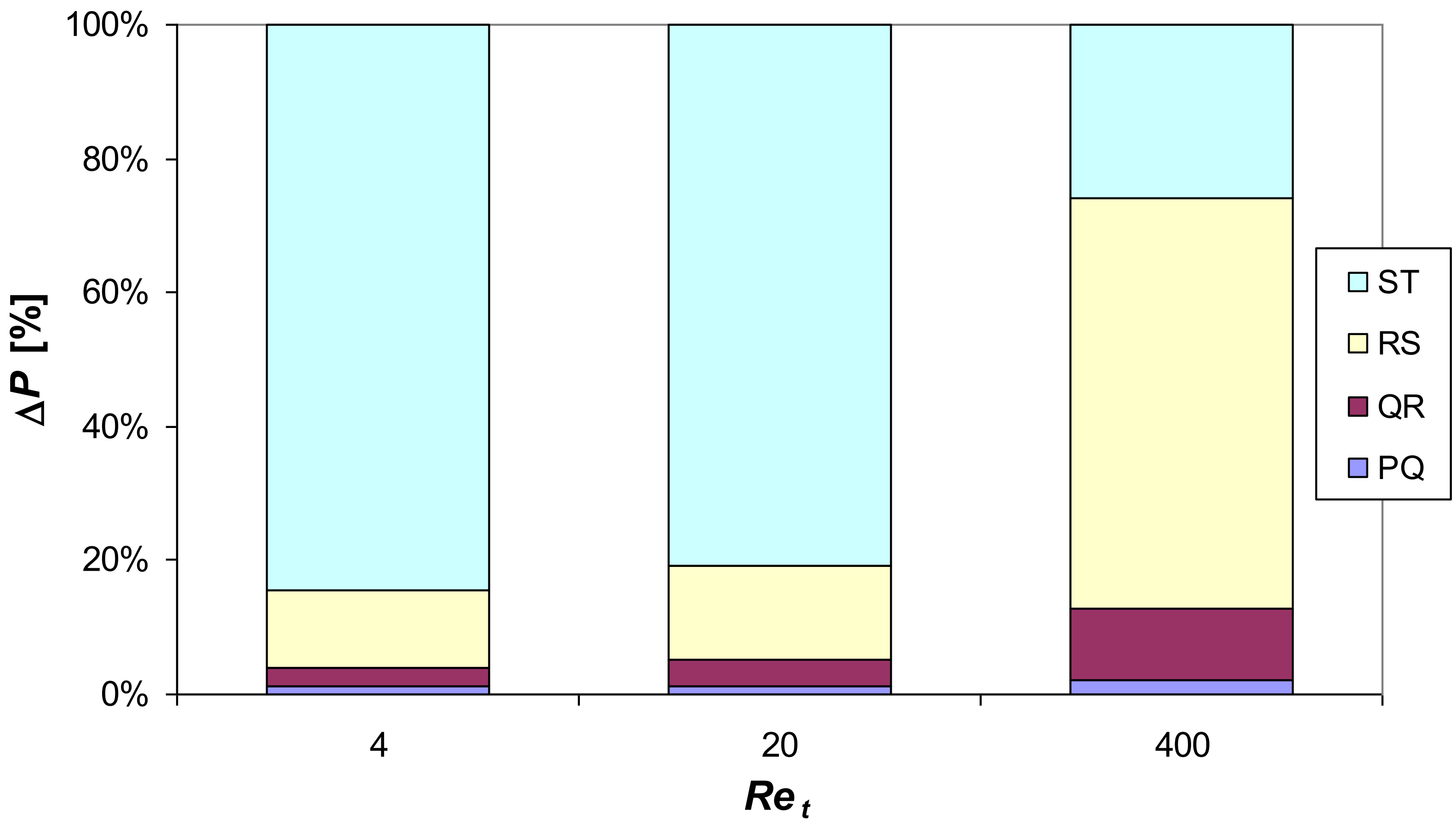

Figure 14 (c): Pressure drop analysis, $h/d_t = 0.65$.

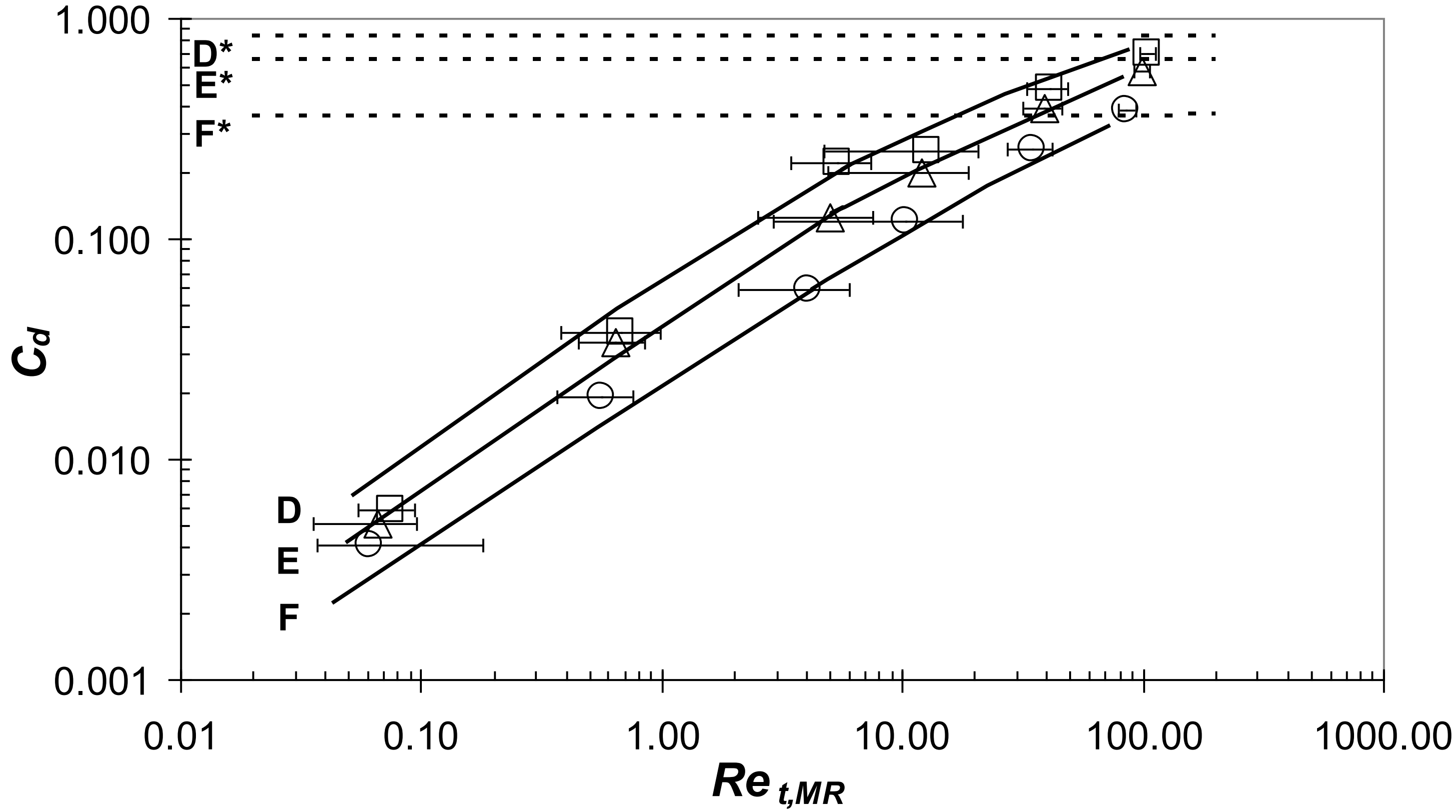

Figure 15: Discharge coefficient versus Re_t for CMC solutions.
Solid lines – this work; **D** – h/d_t = 0.34, **E** – h/d_t = 0.18, **F** – h/d_t = 0.10; symbols – experimental data (Colombo and Steynor, 2002); squares – h/d_t = 0.34, triangles – h/d_t = 0.18, circles – h/d_t = 0.10; dotted lines – empirical model from Tuladhar (2001) – equation (26); **D*** – 0.34, **E*** – h/d_t = 0.18, **F*** – h/d_t = 0.10.
Nozzle: d_t = 2 mm, d = 4 mm, w = 0.2 mm, λ = 0.1 mm and α = 30°.

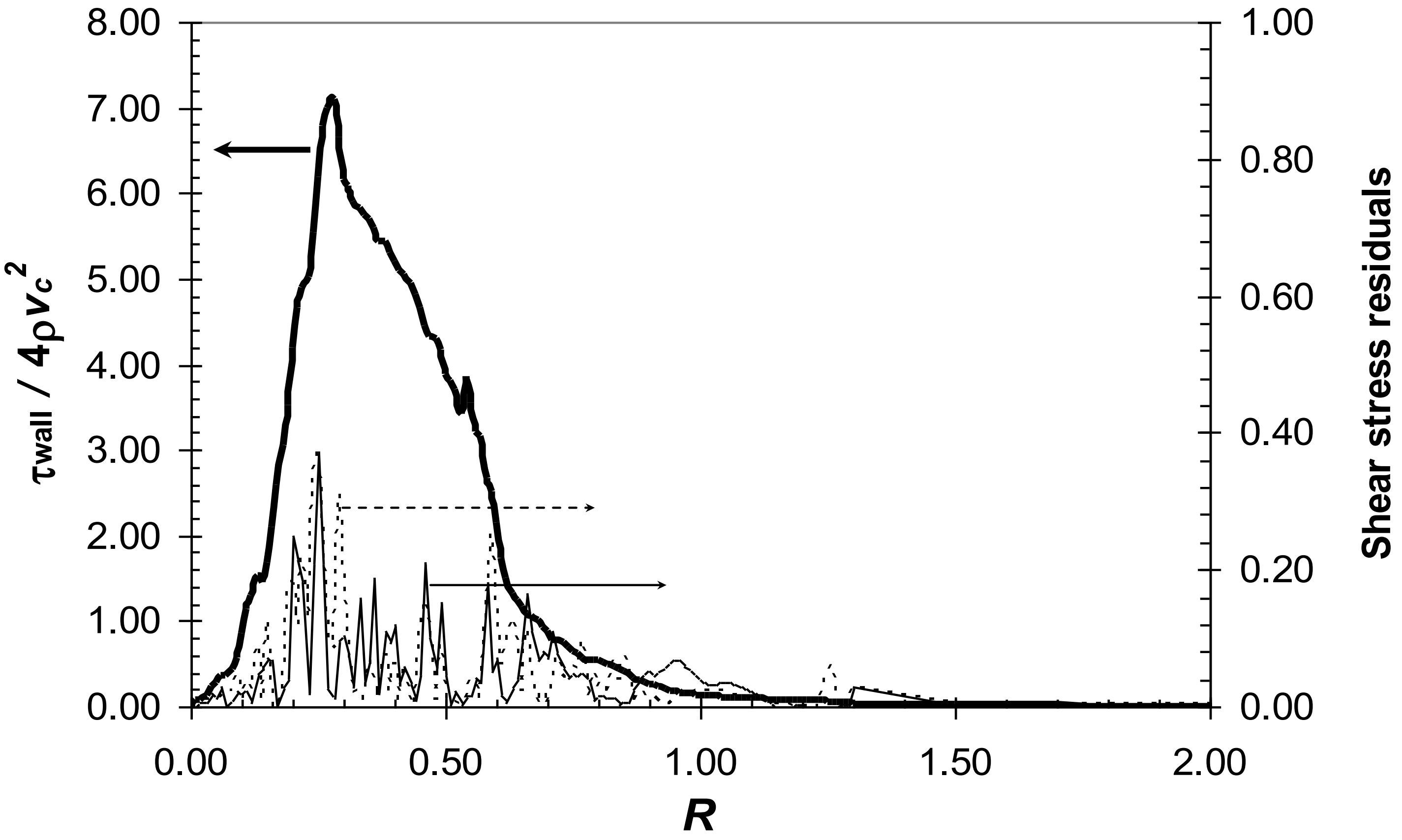

Figure 16(a): Dimensionless shear stress distributions on the gauged surface. Case : $Re_t = 260$, $h/d_t = 0.125$. Thick solid line, Model 1; thin solid line, τ_{wall} residuals (dimensionless) from Model 2 (equation (27)); dotted line, τ_{wall} residuals (dimensionless) from Model 3 (equation (28)).
Nozzle: $d_t = 1.0$ mm, $d = 4.0$ mm, $\lambda = 0.1$ mm and $w = 0.5$ mm.

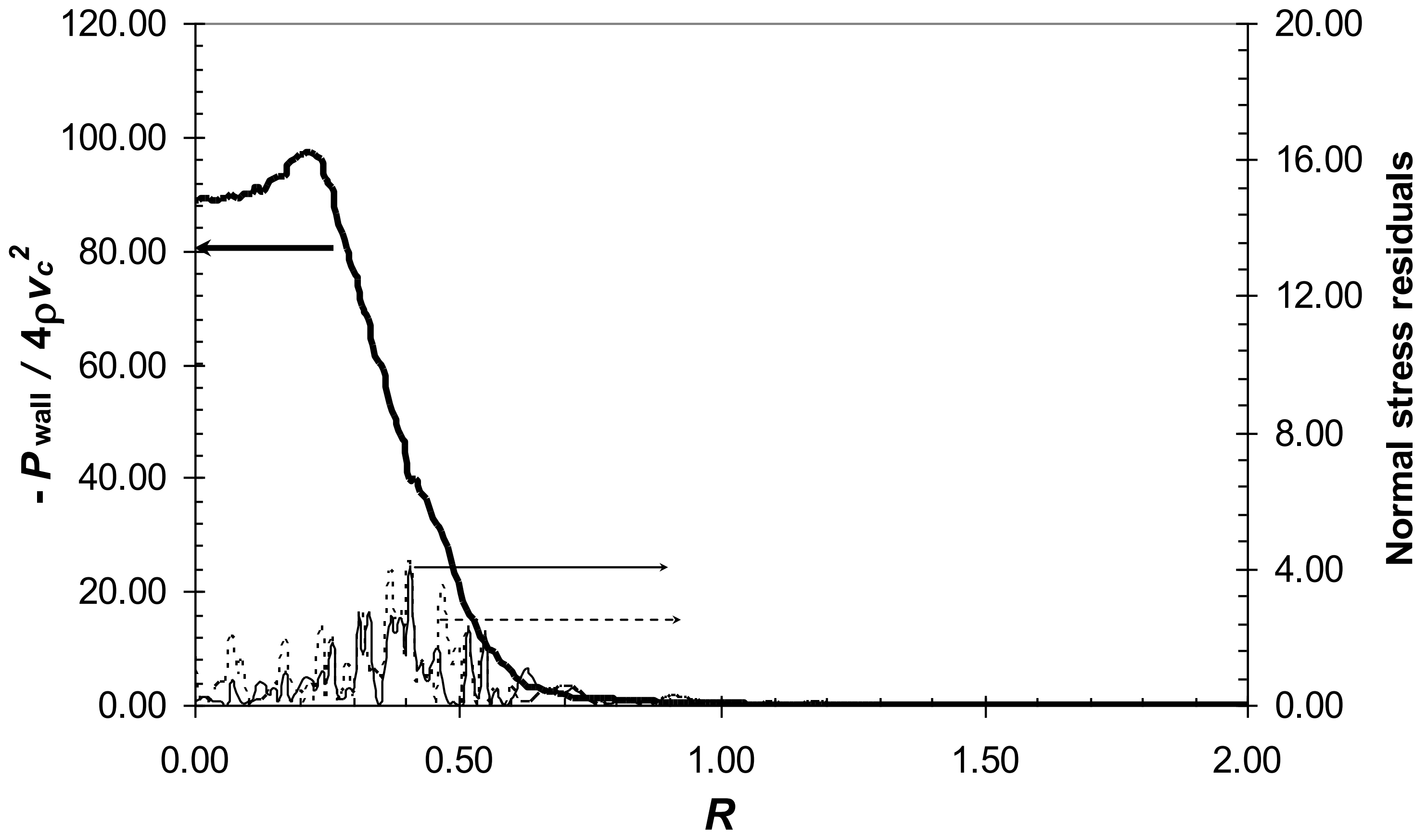

Figure 16(*b*): Dimensionless normal stress distributions on the gauged surface. Case: $Re_t = 260$, $h/d_t = 0.125$.
Thick solid line, Model 1; thin solid line, - P_{wall} residuals (dimensionless) for Model 2 (equation (27)); dotted line, -P_{wall} residuals (dimensionless) for Model 3 (equation (28)).
Nozzle: $d_t = 1.0$ mm, $d = 4.0$ mm, $\lambda = 0.1$ mm and $w = 0.5$ mm.

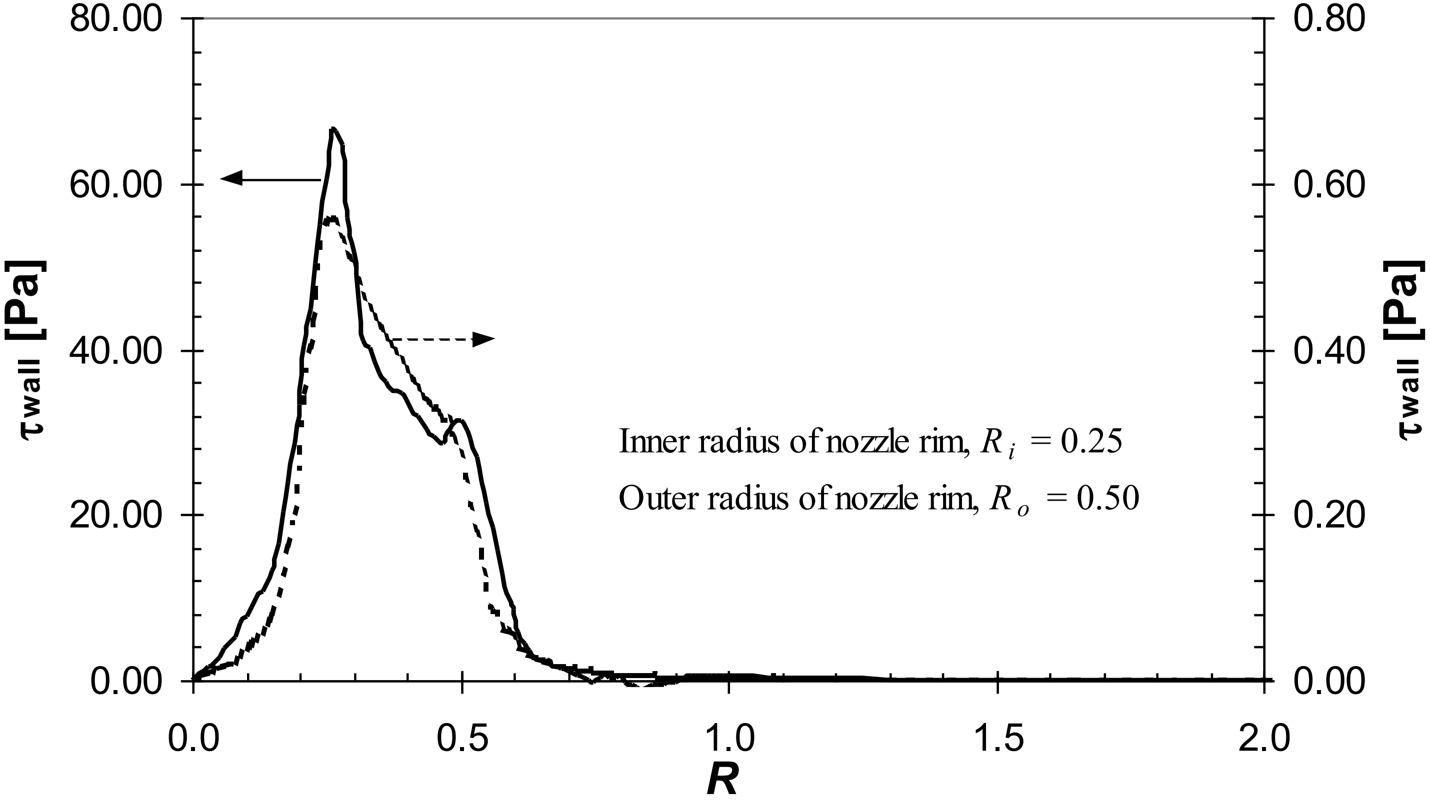

Figure 17(*a*): Shear stress distributions on the gauged surface, Case: $h/d_t = 0.10$. Solid line, $Re_t = 904$; dotted line, $Re_t = 4$.

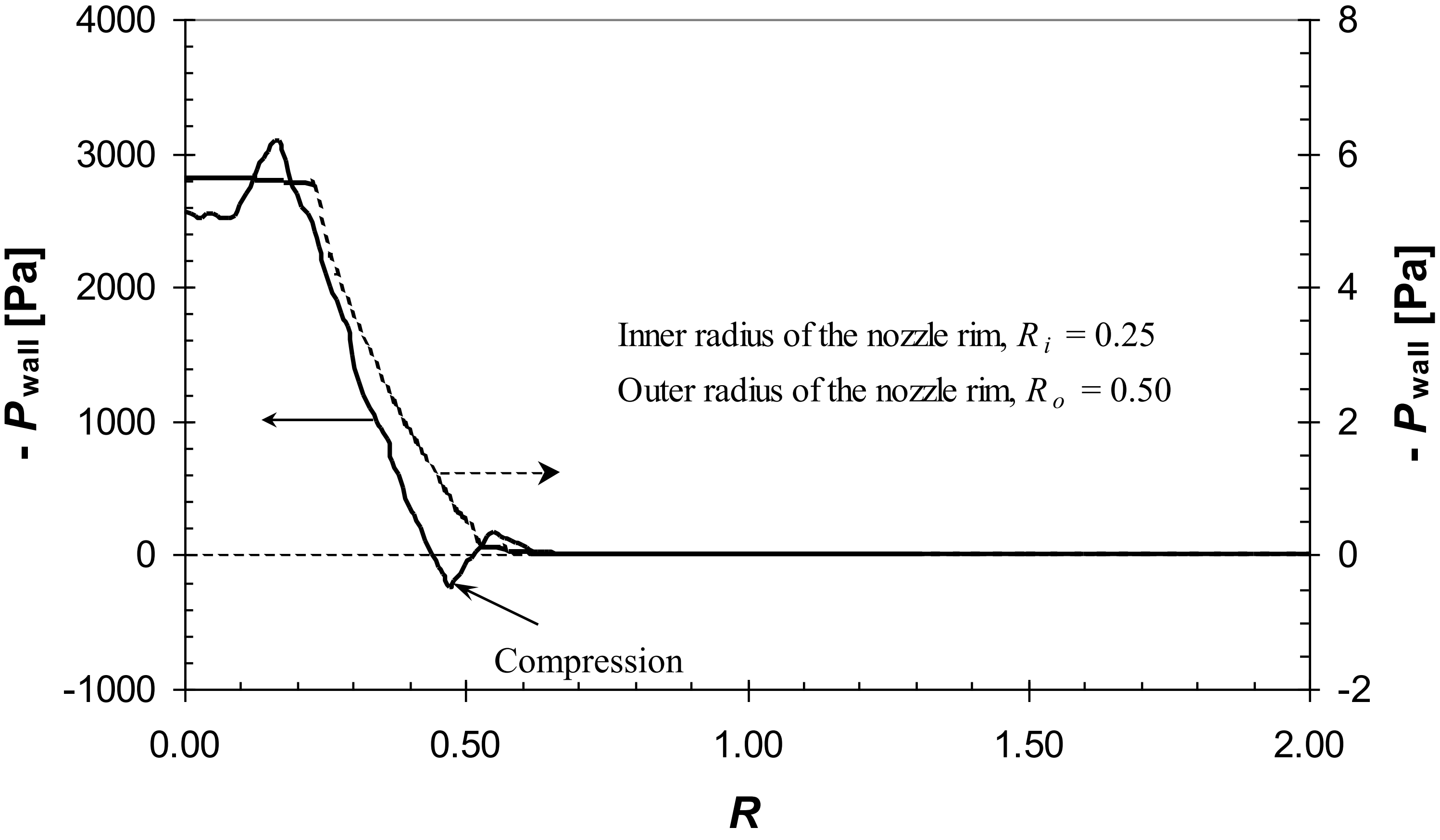

Figure 17(*b*): Normal stress distributions on the gauged surface, Case: $h/d_t = 0.10$. Solid line, $Re_t = 904$; dotted line, $Re_t = 4$.

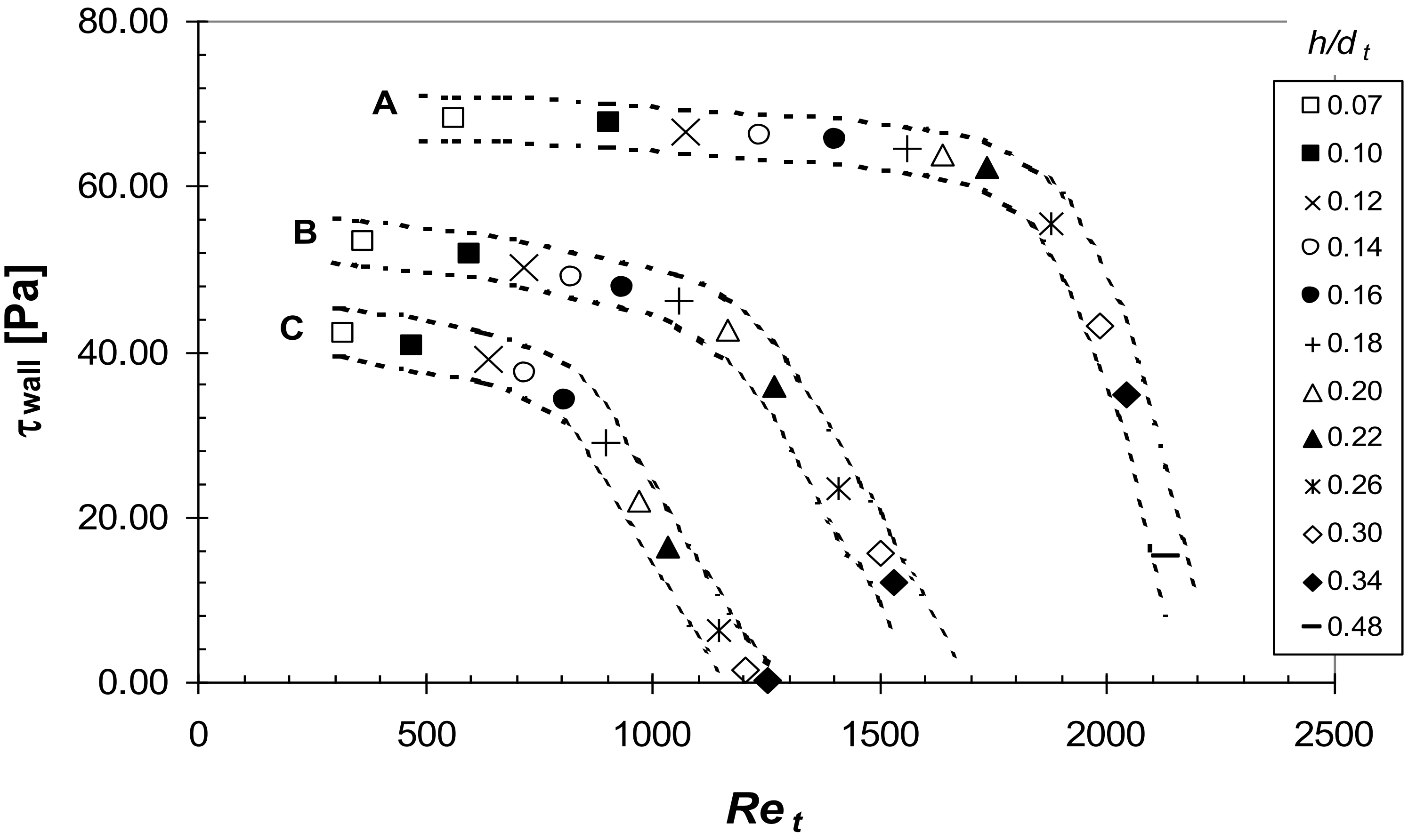

Figure 18: Maximum wall shear stress versus Re_t (water).
Identification of data sets: **A** - s = 340 mm; **B** – s = 200 mm; **C** – s = 140 mm.

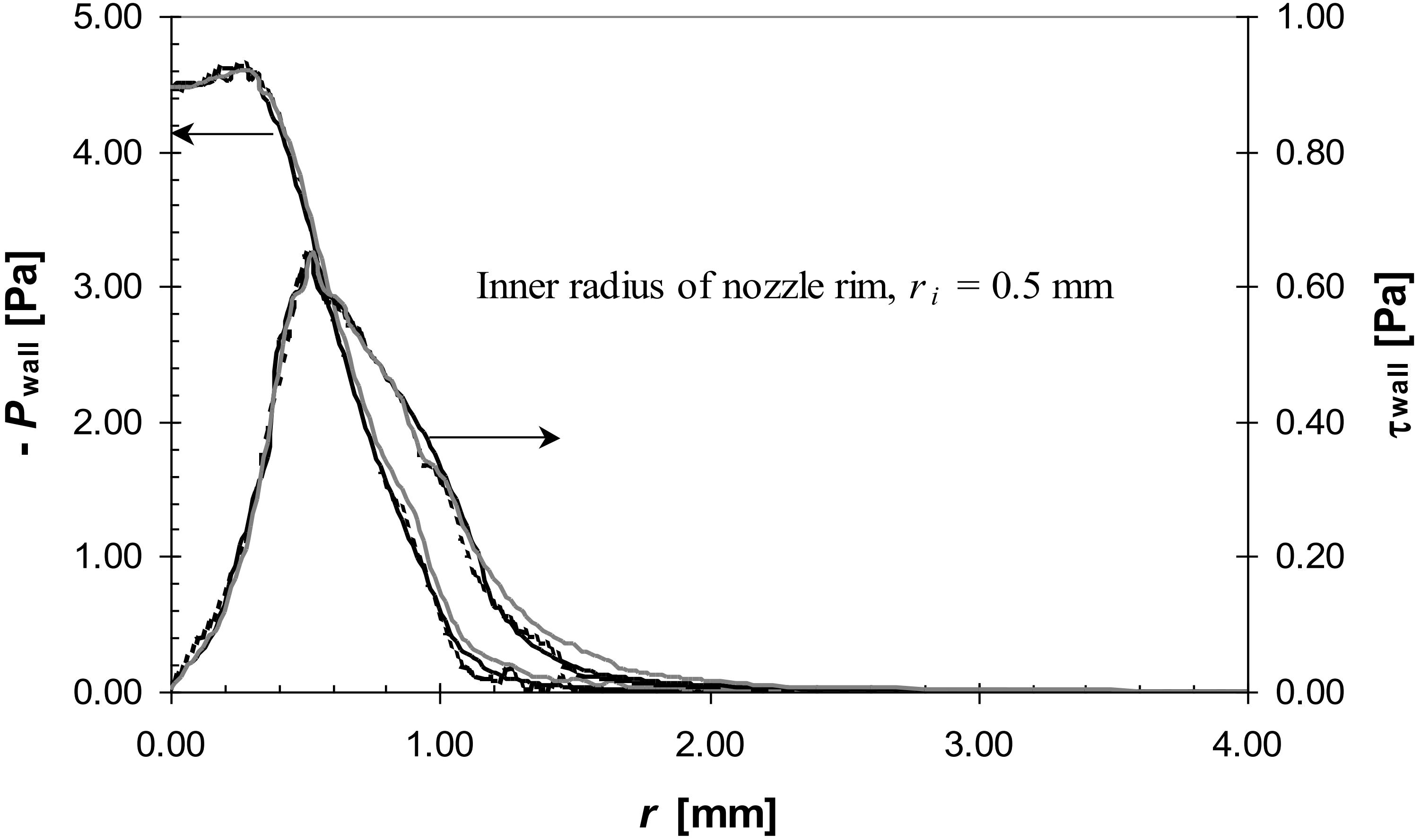

Figure 19(a): Shear and normal stress distributions on the gauged surface, Case: $Re_t = 20$, $h/d_t = 0.20$.
Nozzle: $d_t = 1.0$ mm, $d = 4.0$ mm, $\lambda = 0.1$ mm and $w = 0.5$ mm.
Grey solid line, $\alpha = 60^o$, black solid line, $\alpha = 45^o$, dotted line, $\alpha = 30^o$.

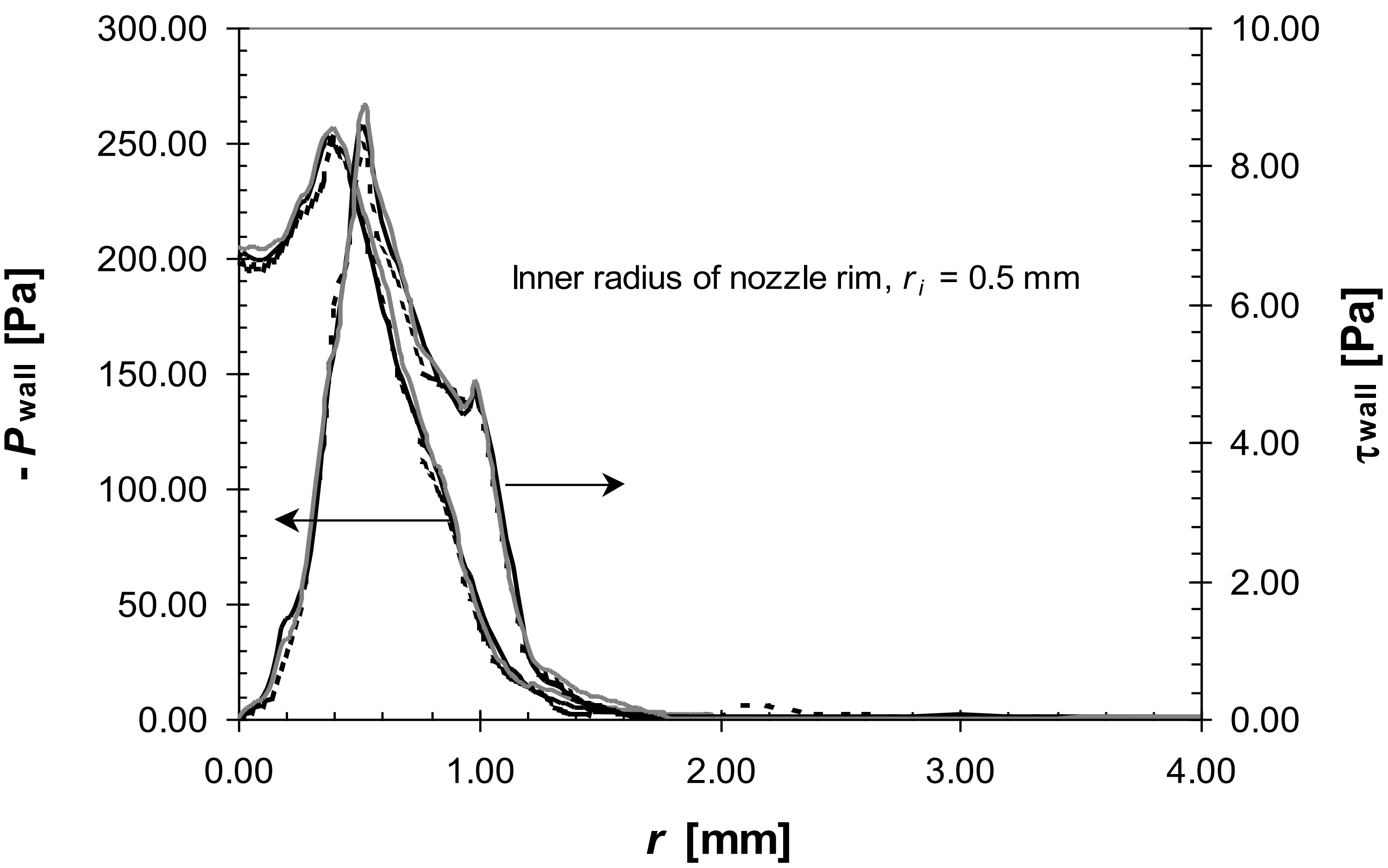

Figure 19(*b*): Shear and normal stress distributions on the gauged surface, Case: $Re_t = 400$, $h/d_t = 0.20$.
Nozzle: $d_t = 1.0$ mm, $d = 4.0$ mm, $\lambda = 0.1$ mm and $w = 0.5$ mm.
Grey solid line, $\alpha = 60^o$, black solid line, $\alpha = 45^o$, dotted line, $\alpha = 30^o$.

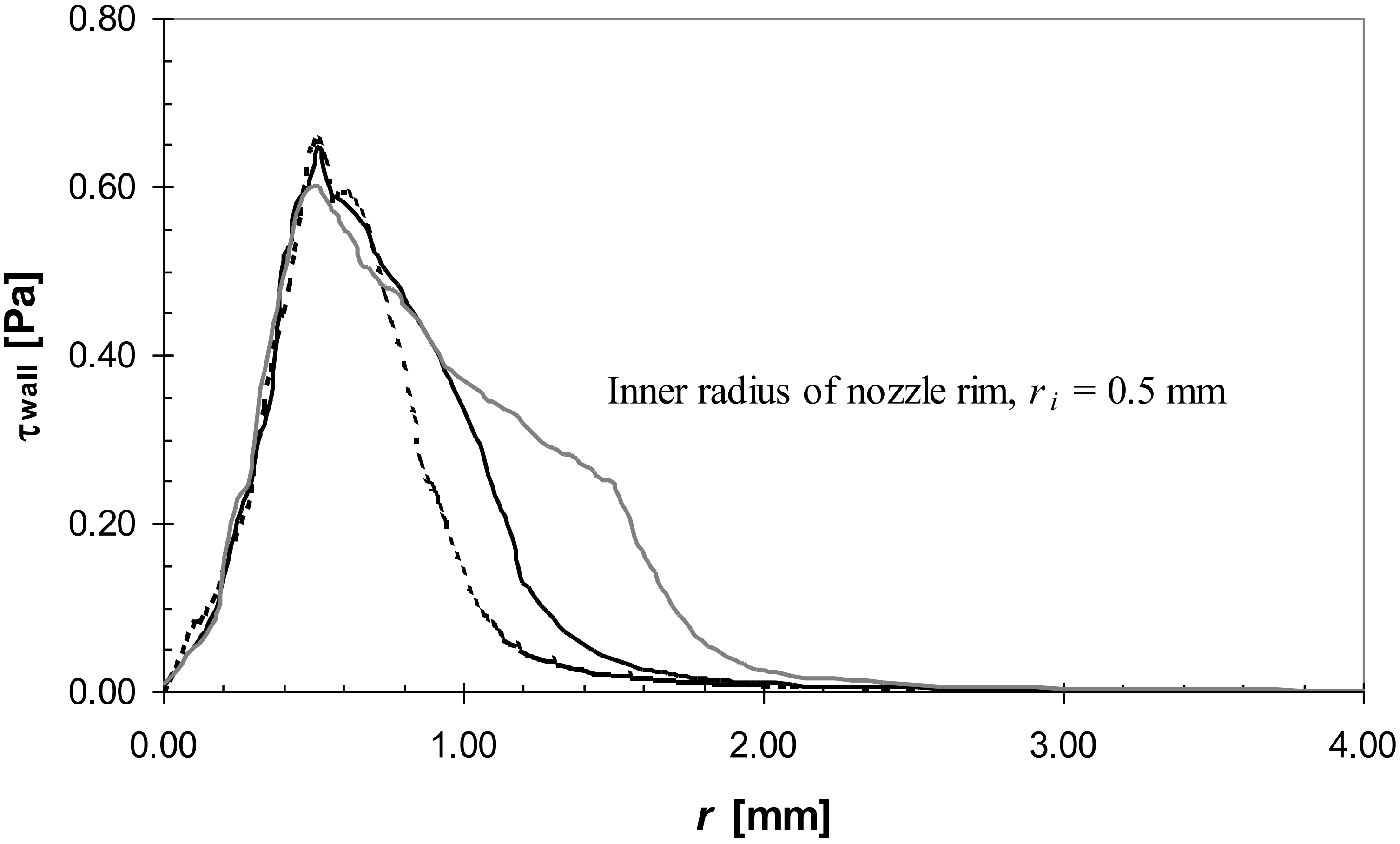

Figure 20(a): Shear stress distributions on the gauged surface, Case: Re_t = 20, h/d_t = 0.20.
Nozzle: d_t = 1.0 mm, d = 4.0 mm, λ = 0.1 mm and α = 45°.
Grey solid line, w = 1.0 mm, black solid line, w = 0.5 mm, dotted line, w = 0.25 mm.

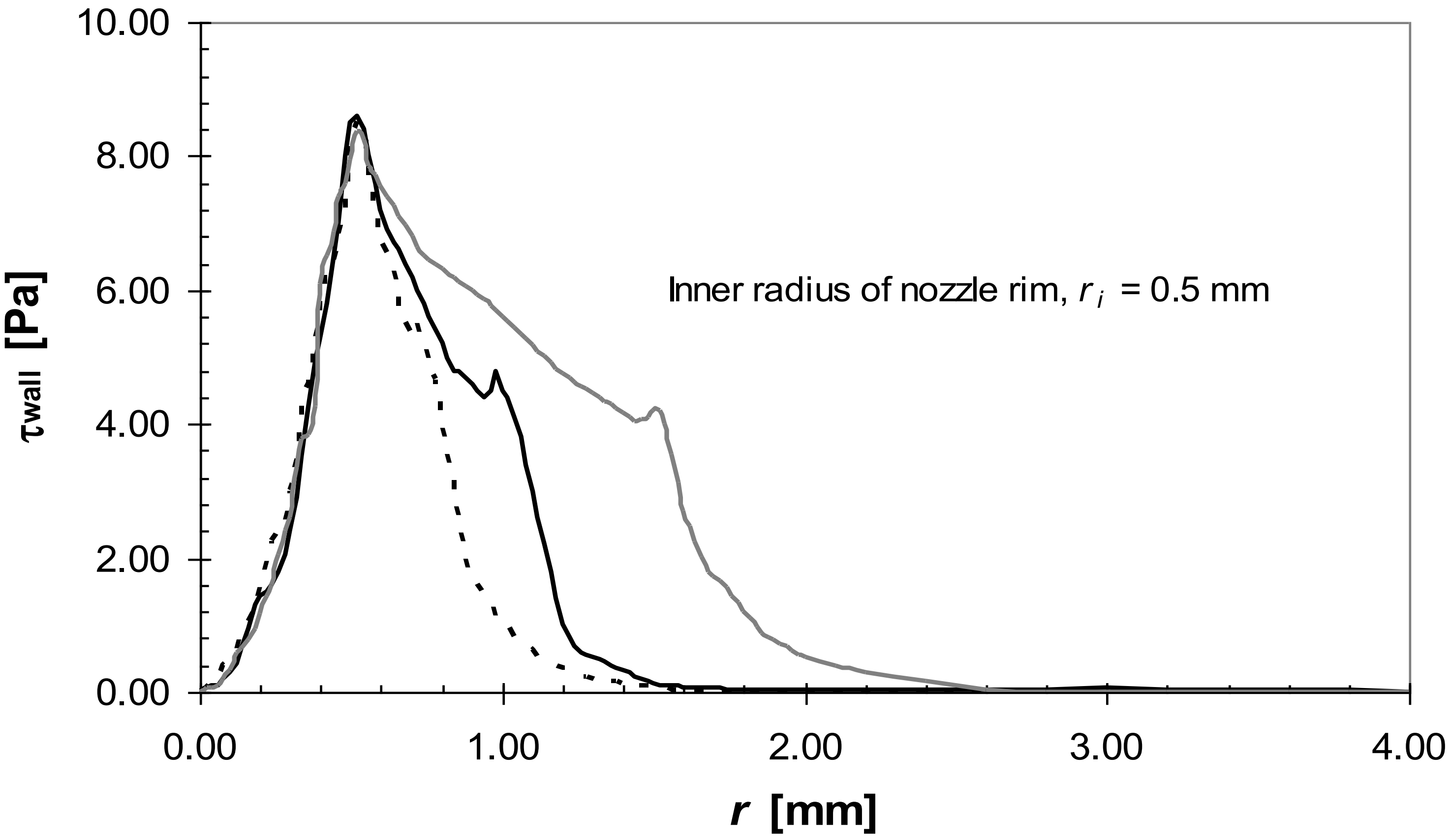

Figure 20(b): Shear stress distributions on the gauged surface, Case: Re_t = 400, h/d_t = 0.20.
Nozzle: d_t = 1.0 mm, d = 4.0 mm, λ = 0.1 mm and α = 45^o.
Grey solid line, w = 1.0 mm, black solid line, w = 0.5 mm, dotted line, w = 0.25 mm.

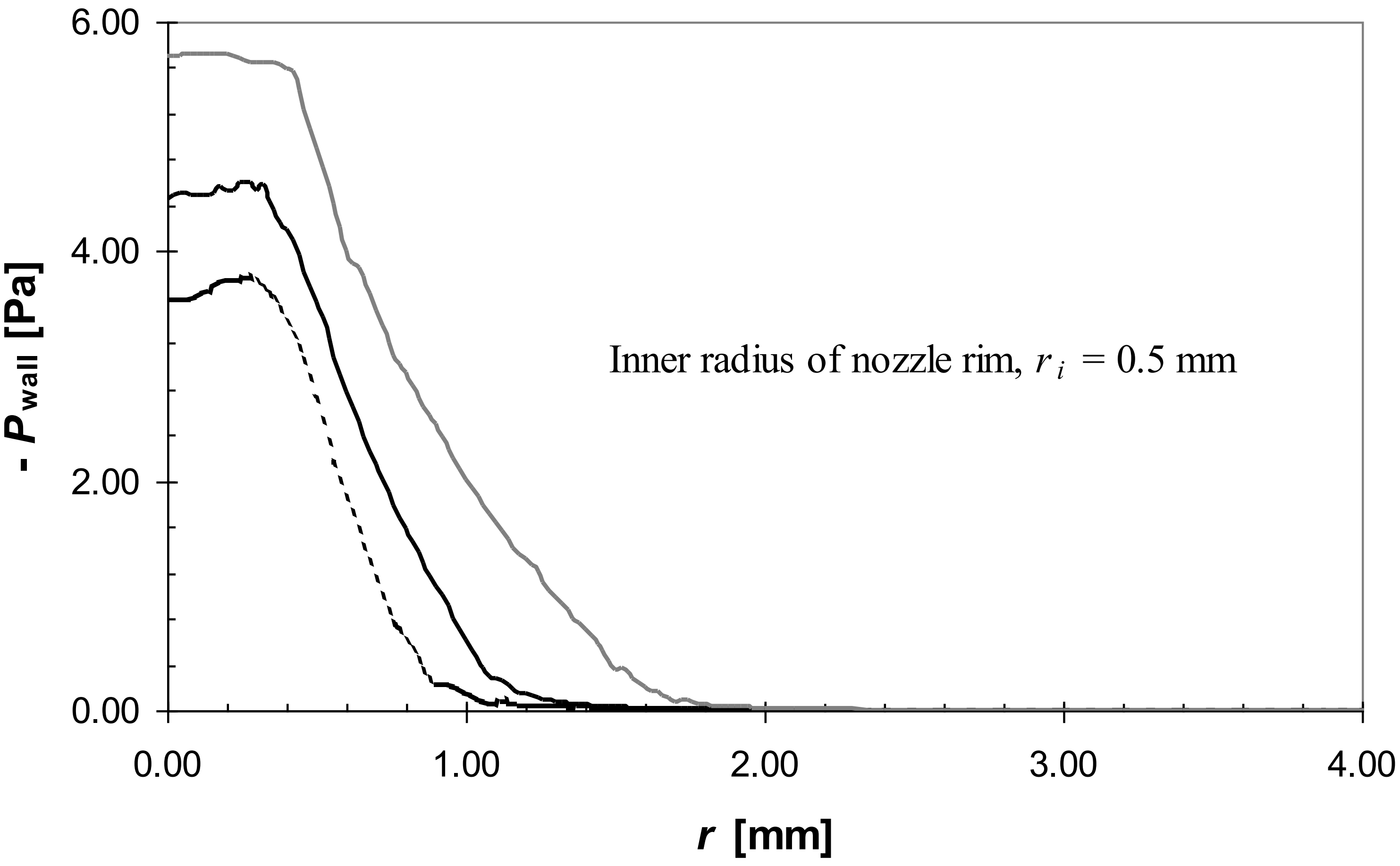

Figure 20(c): Normal stress distributions on the gauged surface, Case: $Re_t = 20$, $h/d_t = 0.20$.
Nozzle: $d_t = 1.0$ mm, $d = 4.0$ mm, $\lambda = 0.1$ mm and $\alpha = 45^o$.
Grey solid line, $w = 1.0$ mm, black solid line, $w = 0.5$ mm, dotted line, $w = 0.25$ mm.

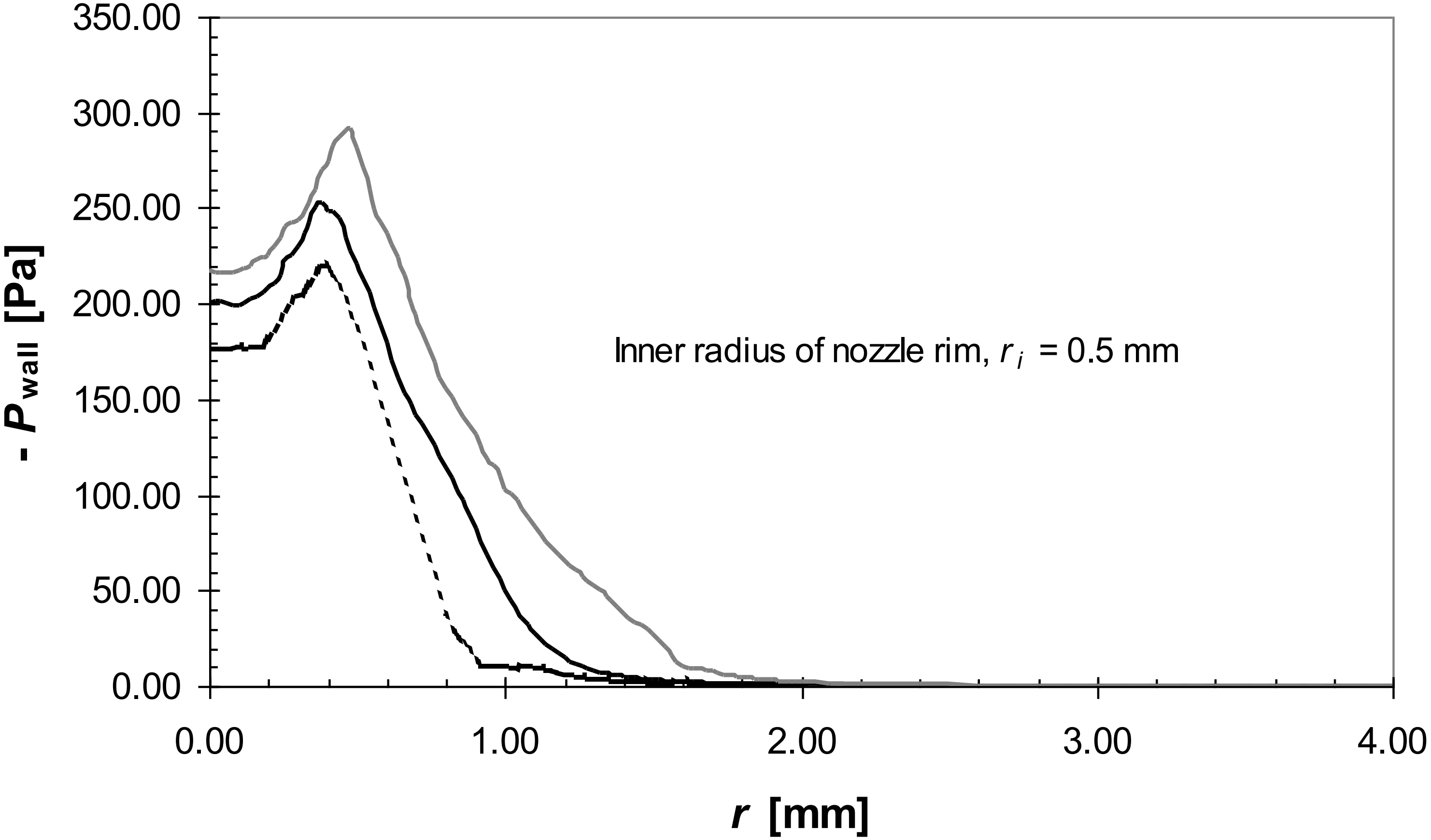

Figure 20 (*d*): Normal stress distributions on the gauged surface, Case: $Re_t = 400$, $h/d_t = 0.20$.
Nozzle: $d_t = 1.0$ mm, $d = 4.0$ mm, $\lambda = 0.1$ mm and $\alpha = 45^{o}$.
Grey solid line, $w = 1.0$ mm, black solid line – $w = 0.5$ mm, dotted line – $w = 0.25$ mm.

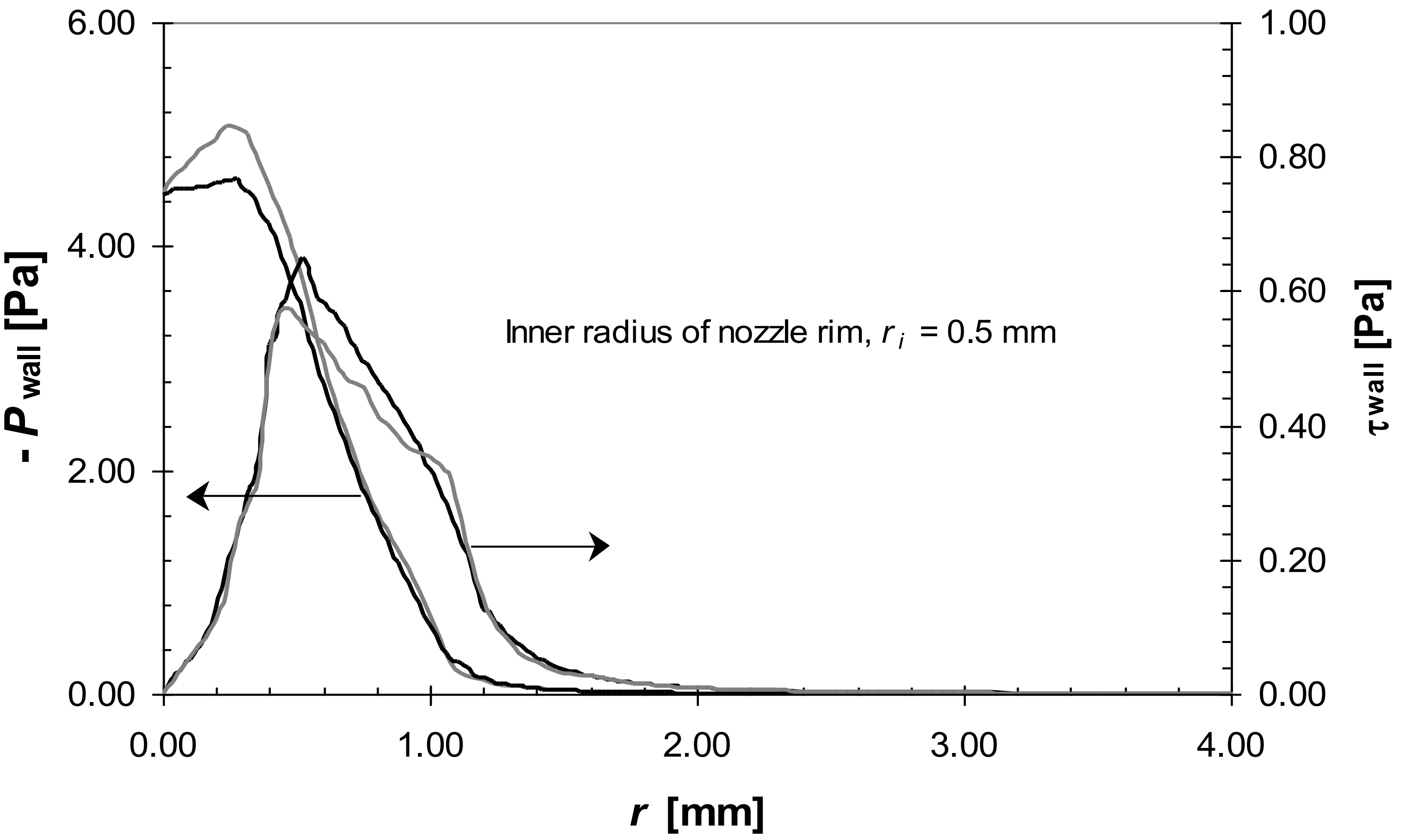

Figure 21 (*a*): Shear stress distributions on the gauged surface, Case: $Re_t = 20$, $h/d_t = 0.20$.
Nozzle: $d_t = 1.0$ mm, $w = 0.5$ mm, $\lambda = 0.1$ mm and $\alpha = 45^o$.
Grey solid line, $d = 8.0$ mm, black solid line, $d = 4.0$ mm.

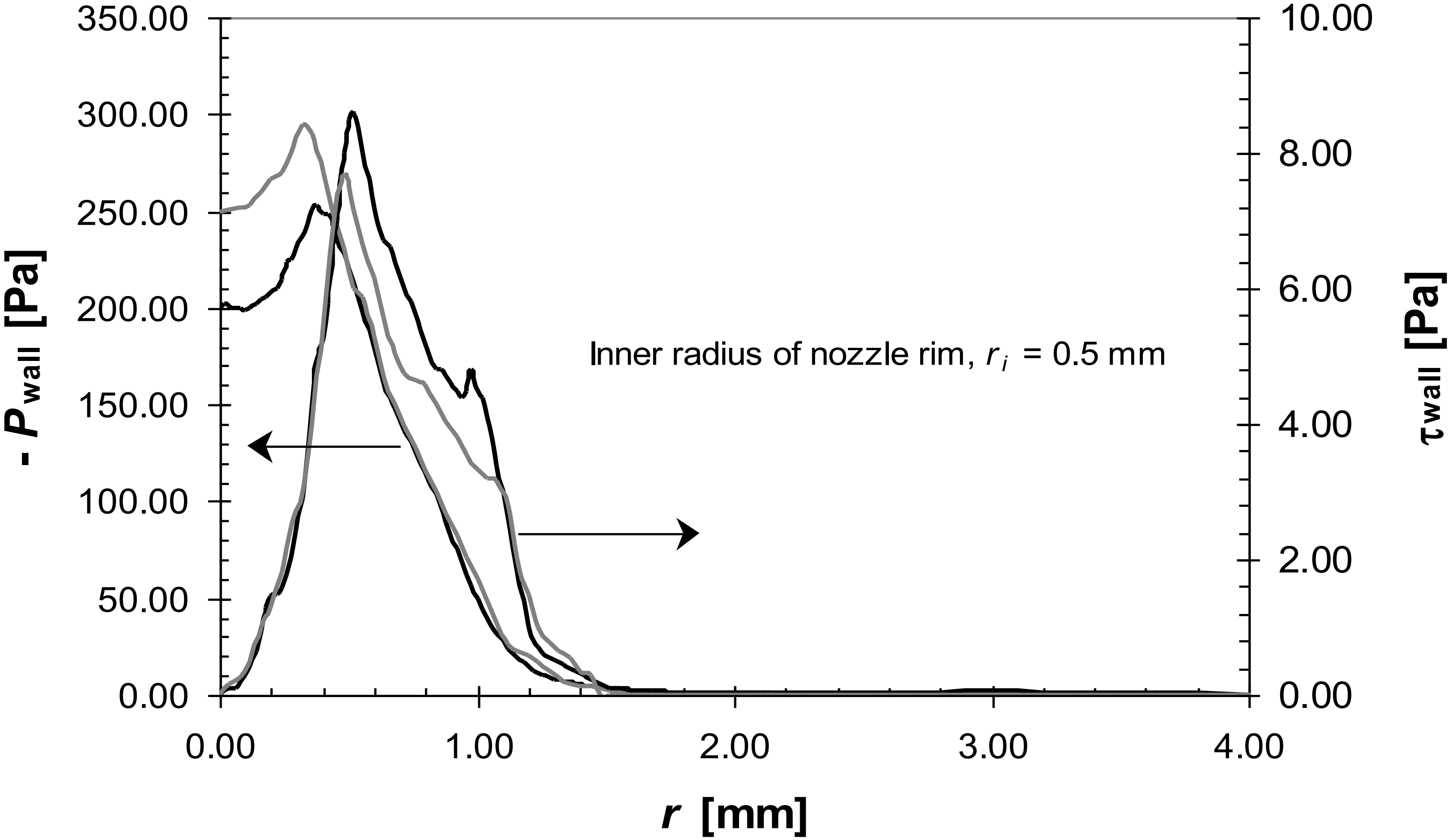

Figure 21 (*b*): Shear stress distributions on the gauged surface, Case: $Re_t = 400$, $h/d_t = 0.20$.
Nozzle: $d_t = 1.0$ mm, $w = 0.5$ mm, $\lambda = 0.1$ mm and $\alpha = 45^o$.
Grey solid line, $d = 8.0$ mm, black solid line, $d = 4.0$ mm.

	$0 \leq \boldsymbol{Re_t} \leq 200$	$201 \leq \boldsymbol{Re_t} \leq 1000$	$1001 \leq \boldsymbol{Re_t} \leq 1500$	$1501 \leq \boldsymbol{Re_t} \leq 2200$
$0.07 \leq \boldsymbol{h/d_t} \leq 0.10$	$30 \times R_{tube}$	$90 \times R_{tube}$	–	–
$0.11 \leq \boldsymbol{h/d_t} \leq 0.20$	$30 \times R_{tube}$	$100 \times R_{tube}$	$130 \times R_{tube}$	–
$0.21 \leq \boldsymbol{h/d_t} \leq 0.30$	$30 \times R_{tube}$	$90 \times R_{tube}$	$110 \times R_{tube}$	$130 \times R_{tube}$
$0.31 \leq \boldsymbol{h/d_t} \leq 0.50$	$20 \times R_{tube}$	$70 \times R_{tube}$	$100 \times R_{tube}$	$110 \times R_{tube}$
$0.51 \leq \boldsymbol{h/d_t} \leq 0.65$	$20 \times R_{tube}$	$70 \times R_{tube}$	$100 \times R_{tube}$	$110 \times R_{tube}$

Table 1: Summary of the values of L_1 used in the simulations.

Sucrose solution (w/w %)	Viscosity (kg/ms)	
	Experimental	Mathlouthi and Genotelle (1995)
15%	0.00145	0.00140
25%	0.00224	0.00215
35%	0.00373	0.00374

Table 2: Summary of the viscosities for sucrose solutions at 25^{o}C.

- 0.34

CMC solution (w/w %)	*n*	*k*
0.8% high viscosity	0.59	0.60
0.5% high viscosity	0.61	0.40
0.3% high viscosity	0.67	0.18
0.8% low viscosity	0.85	0.033
0.5% low viscosity	0.93	0.0106
0.3% low viscosity	0.98	0.0044

Table 3: Summary of the rheological parameters for CMC solution at 25^{o}C (Colombo & Steynor, 2002).